Advancing the Kinetics Model in OpenSim for Human Motion Estimation Based on IMUs

Performance Analysis with Wheelchair User Motion

X. Tang

TUDelft
Delft
University of
Technology

Delft Center for Systems and Control

Advancing the Kinetics Model in OpenSim for Human Motion Estimation Based on IMUs

Performance Analysis with Wheelchair User Motion

MASTER THESIS

X. Tang

August 17, 2023

Faculty of Mechanical, Maritime and Materials Engineering (3mE) · Delft University of Technology

BioMechanical
Engineering

TU Delft

Delft
University of
Technology

DCSC

Abstract

Inertial Measurement Units (IMUs) have become increasingly popular in human motion estimation due to their portability, self-contained features, and cost-effectiveness compared to marker-based sensing systems which rely on external cameras to observe the position of the markers. Over the years, many studies have proposed various models and algorithms based on IMUs and the kinematics of the human body for motion estimation, neglecting the fact that IMUs measure acceleration, which can be directly related to joint torque with known inertial parameters. In turn, by estimating joint torque and incorporating kinetics into the model, it becomes possible to address a long-standing problem in biomechanics: the marker-based sensing system's inability to provide a reliable estimation of kinetics due to the need for numerical differentiation. In a previous study, a kinetics model was proposed for estimating the motion but validated only on a robotic arm. In our study, we further explore the performance of using IMUs to estimate wheelchair user motion data based on Extended Kalman Filter (EKF) and the kinetics model, with marker-based Inverse Kinematics (IK)/Inverse Dynamics (ID) as the benchmark.

Compared to Marker-based IK, the method leveraging kinetics achieves a Root Mean Squared Difference (RMSD) below 16° for three out of four tasks across all joints throughout the trial. After analyzing the only task with degradation in estimation, we conclude that the erroneous IMUs measurements results from Soft Tissue Artefacts (STA) is the most likely reason. For joint torque estimation, the RMSD for joint torque estimation is below 3.05Nm for the tasks less affected STA. Through fine-tuning the EKF, we can achieve fast and responsive estimation results without being affected by numerical differentiation, enabling us to capture both sudden and subtle changes in joint torque estimation. The kinetics model performs better than the kinematics-based model in estimating both kinematics and kinetics and also reduces drifting behavior. Compared to OpenSense, which depends on magnetometer measurements, kinetics model estimation shows comparable kinematics estimation accuracy while excluding the use of heading information. The results show that including the kinetics model for human motion estimation can improve estimation accuracy and robustness encouraging further studies to include kinetics for human motion estimation.

Table of Contents

List of Figures

List of Tables

Preface

From a young age, I have always been bursting with energy, indulging in a variety of sports ranging from football to basketball. As time went on, my interests shifted, and I found myself drawn towards sculpting my physique as a bodybuilder. However, throughout this journey, one particular obstacle has plagued me: my lack of flexibility. The excruciating pain I endured during Taekwondo sessions, as the coach applied pressure to stretch my leg, still lingers in my memory. Even today, the frustration persists as I struggle to perform a proper deep squat due to my limited flexibility.

When I first discovered the potential of utilizing IMUs to estimate human body motion, I was like: "I'm in." The prospect of making a modest contribution to this field and, perhaps, advancing our ability to accurately measure the forces exerted on each segment of the body filled me with excitement. Who knows? In doing so, we may eventually unlock valuable insights into analyzing and addressing the very flexibility issues that have personally plagued individuals like myself.

Acknowledgements

I would like to express my deepest gratitude to my main supervisors, Manon Kok and Ajay Seth, whose brilliance and guidance have been invaluable throughout this journey. Their insightful advice provided during our meetings has kept me on the right track, and our engaging discussions have been truly enlightening. I'm like a Gaussian process with a large covariance, thanks to their unwavering support I can consistently converged towards my goals,

I would also like to extend my sincere appreciation to my daily supervisor, Li Ruiyuan, and my dataset supporter Wiebe de Vries, for the invaluable advice provided on thesis writing and the patient answers to my question to the dataset.

I would like to express my sincere gratitude to all the individuals from the Sensor Fusion Group at DCSC and the Biomechanical Engineering group at CBL. This project represents a unique fusion of two distinct fields, and your engaging and insightful contributions during the meetings have not only enriched my understanding of both areas of study but also sparked my further intrigue and exploration.

I would like to extend a special acknowledgment to Phoebe Gu, David Fu, William Zhang, Hendrik Jaap Algra, Dong, Tony, and numerous others who have provided unwavering support and encouragement throughout my master's journey. Your presence and support have played a crucial role in my academic and personal growth, and I am truly grateful for your companionship throughout my master's journey.

Last but certainly not least, I want to express my deepest gratitude to my mom and dad. Their unwavering love and support, spanning across half the globe, have made me feel like I always have the strongest backing wherever I go in the world.

Delft, University of Technology
August 17, 2023

X. Tang

"我就是为了这点儿醋, 才包的这顿饺子。

I make dumplings just to savor the vinegar."

— 蓝青峰, 邪不压正，2018

Glossary

List of Acronyms

MEKF	Multiplicative Extended Kalman Filter
RMSD	Root Mean Squared Difference
LG-EKF	Extended Kalman Filter on Lie Groups
DH	Denavit–Hartenberg
MMH	Manual Material Handling
MD	Mean Absolute Difference
DoF	Degrees of Freedom
IMU	Inertial Measurement Unit
IMUs	Inertial Measurement Units
IK	Inverse Kinematics
ID	Inverse Dynamics
UKF	Unscented Kalman Filter
EKF	Extended Kalman Filter
IEKF	Iterative Extended Kalman Filter
EoM	Equations of Motion
STA	Soft Tissue Artefacts
BLM	Bony Landmark

List of Symbols

Q_τ	Generalized force prediction noise covariance matrix
$\bar{\mathbf{Q}}$	Gravity-induced forces projected on to generalized coordinates
$\bar{f}_{const}$	Constant term left due to linearization and discretization

$\ddot{\boldsymbol{q}}$	Generalized acceleration
$\dot{\boldsymbol{q}}$	Generalized velocity
$\boldsymbol{\tau}$	Generalized force/torque
$\boldsymbol{e}$	Measurement noise
$\boldsymbol{q}$	Generalized coordinates
$\boldsymbol{v}$	Process noise
$\boldsymbol{x}$	System states vector
$\hat{\boldsymbol{x}}_{k|k}$	State estimation of Kalman filter
$\hat{\boldsymbol{x}}_{k+1|k}$	State estimation of prediction
$\mathbf{C}(\boldsymbol{q}, \dot{\boldsymbol{q}})$	Coriolis and centrifugal forces
$\mathbf{M}$	Generalized mass matrix
$\mathbf{Q}$	Forces and torques projected on to generalized coordinates
$A_{\boldsymbol{x}_k}$	Linear system dynamic model
$B_{\boldsymbol{v}, \boldsymbol{x}_k}$	Linear system noise dynamic model
$B_{u, \boldsymbol{x}_k}$	Linear system input dynamic model
$F_{\boldsymbol{x}_k}$	Discrete system dynamic model
f_{const}	Constant term left due to linearization
f_{ext}	Applied external forces
$h(\boldsymbol{x})$	System measurement model
$H_{\boldsymbol{x}}$	Jacobian of system measurement model
J	Multibody system Jacobian
J_v	Multibody linear system Jacobian
J_ω	Multibody angular system Jacobian
$L_{\boldsymbol{v}, \boldsymbol{x}_k}$	Discrete system noise dynamic model
$L_{u, \boldsymbol{x}_k}$	Discrete system input dynamic model
$P_{k|k}$	Covariance matrix after correction in Kalman filter
$P_{k+1|k}$	Prediction covariance matrix in Kalman filter
$Q_{\boldsymbol{q}}$	Generalized coordinates prediction noise covariance matrix
Q_f	Generalized velocity prediction noise covariance matrix, which also represents the noise covariance of the external force measurements
R	Measurement noise covariance matrix
Y_k	All past system measurements up to step k
${}^{s_i}J_{s_i, \omega}$	Multibody angular Jacobian of the ith IMU
${}^{s_i}J_{s_i, v}$	Multibody linear Jacobian of the ith IMU
${}^{s_i}y_{\mathrm{a}}$	Specific force measurement from the ith IMUs
${}^{s_i}y_{\omega}$	Angular velocity measurement from the ith IMUs

Chapter 1

Introduction

1-1 Background

The elegance and intricacy of human motion are truly captivating. From the exhilarating sprinter dashing across the track to the graceful rotations of a ballet dancer, the beauty of human movement is undeniable. By quantitatively capturing and analyzing human motion, we can unlock a multitude of benefits across various fields.

In the realm of sports and athletics, precise human motion estimation empowers performance evaluation, technique refinement, injury prevention, and optimization of training strategies [1, 2]. In the realm of ergonomics, capturing accurate human motion data becomes instrumental in designing workspaces, equipment, and tools that minimize the risk of musculoskeletal disorders and optimize human performance [3, 4, 5]. Moreover, the ability to faithfully replicate natural human movements through accurate motion estimation further enhances the realism and believability of the animations and simulations.

However, quantitatively capturing human motion is no easy feat. It involves the intricate coordination of multiple body segments, requiring precise and dynamic motor control mechanisms [6]. With numerous joints possessing unique flexibility, range of motion, and interactions with muscles and ligaments, the complexity of human motion deepens.

1-1-1 Sensors

To estimate human motion, we need a sensing system to record meaningful information on the human body. Optical motion capture is commonly used for human motion analysis, which is limited to indoor settings and restricts the range of activities that can be captured within the camera's field of view. This confinement of human activity within a limited space diminishes the credibility of the data. Therefore, the challenge lies in developing robust methodologies to effectively capture and analyze these intricate movements without any confinement to human motion. Inertial Measurement Unit (IMU) is a popular alternative to the marker-based sensing system, which will be introduced in the following section.

Marker Markers are passive and reflective sensors attached to specific anatomical landmarks or objects on the body. These markers serve as reference points and enable the tracking and analysis of human movement. Markers are typically lightweight and non-intrusive. During motion capture, multiple cameras are needed to observe the positions of markers in three-dimensional space. By locating and tracking markers on the body, the movement trajectory of the body segments and kinematic parameters, such as joint angles, joint velocities, and segment positions, can be estimated [7].

IMU IMU combines the accelerometer and gyroscope sensors to measure and track the motion and orientation of an object in three-dimensional space [8].

  (1) Accelerometer: The accelerometer quantifies the specific force, which includes both the acceleration experienced by the sensor and the gravitational force.
  (2) Gyroscope: The gyroscope measures the angular velocity of an object around its three axes. It provides information about the rate of change of orientation.

Studies have been trying to use Inertial Measurement Units (IMUs) as a substitute for the widely used marker-based sensing system, as IMUs offer advantages such as portability, free from the occlusion problems as in marker-based sensing systems [9], and the ability to operate in various environments. In the context of human motion analysis, by tracking the raw signals or orientations of the IMUs attached to body segments, it is possible to estimate the motion of the human body. Studies have designed various models and algorithms to achieve human motion capture using IMU.

1-1-2 Models

The accuracy of the model in representing the realistic human body, in terms of anatomical realism, is always a subject of debate. The term "biofidelity" is used to describe the degree to which a model accurately represents and reflects the characteristics and behavior of the real biological system. In the task of human motion estimation, the model of the human body needs to be defined such that all the states in the model are identifiable based on the measurement system.

For example, the shoulder mechanism, comprising the thorax, clavicle, scapula, and humerus, is widely recognized as one of the most complex systems in musculoskeletal modeling due to its intricate nature [10]. F. Helm proposed a comprehensive model for the shoulder [10], encompassing four skeletal structures, three joint connections, three ligaments, the scapulothoracic gliding plane, and a total of 20 muscles and muscle segments [10]. In our study, we will not focus on the muscle of the human body. Therefore, a marker-based sensing system could utilize redundant markers on all shoulder segments, enabling the identification of all kinematic variables. On the other hand, studies limited to a small number of IMUs placed only on the humerus and thorax segments around the shoulder joint typically focus solely on the glenohumeral joint mechanism [11, 12, 13, 14]. Therefore, researchers often adjust the complexity of the model to suit their specific study requirements.

Although many studies have reduced the number of joints used in their model to make all the states identifiable, they also try to increase their biofidelity and estimation accuracy by introducing more estimation variables and constraints. In the studies by M. Kok et al. [15],

the sensor alignment parameters, sensor bias, and the constraints of common joints between two segments were used in the model. A similar approach was proposed by T. McGrath et al. [16], where complex anthropometry constraints were included. Even though more complex constraints were used in their model, under certain circumstances the states of the system still might become non-identifiable [16, 17] due to the lack of heading information in the system.

Among the previous studies of human motion estimation, the work of E. Dorschky [18] using kinetics for human motion estimation has inspired the basis of our study. They have embodied muscle activation as the state of the system for estimating both kinematics and kinetics. However, their model is only in 2-dimensional space and the analysis of the estimation accuracy is only conducted to the wrapped gait cycle. This has weakened the generality of their study. In the work of De. Kanter [19], the model definition has taken one step back by excluding the muscle force but using a kinetics model, which is used for estimating both kinematics and kinetics. The method of De. Kanter [19] shows promising accuracy with validation on robotic arms. However, when defining a model for robotic arms, unlike the model approximated for the human body, the robotic arm model can be obtained with a high degree of accuracy. In contrast, when dealing with the human body model, it becomes challenging to achieve the same level of precision. Therefore, the model incorporating kinetics knowledge still requires testing on the human body, where an accurate definition of the model is more difficult to achieve compared to robotic arms.

1-1-3   Estimation Algorithms

When analyzing human motion, the reason why we needed an estimation algorithm is that the variables our interests, such as joint torque, usually can not be directly measured. Based on the measurements that can be provided by the sensing system and the model tailored suitable for estimation, the algorithm for estimating the variables of our interests also needs to be designed.

When the model is parametrized using the Euler angle to represent the motion of the human body, studies have employed standard Extended Kalman Filter (EKF) [12]. However, modifications have been applied to accommodate different models, e.g. Iterative Extended Kalman Filter (IEKF) [19] and Unscented Kalman Filter (UKF) [11] have also been used considering the nonlinearity of the model. In the work of I. Weygers et al. [14], the biomechanical model is defined as a series of body segments connected by common joint constraints [17]. Each segment's orientation is represented using quaternions, and the Multiplicative Extended Kalman Filter (MEKF) [20] is employed with orientation deviation as the state variable, as quaternions do not lie in Euclidean space. The orientation of each segment can also be used as the system's state variable [13], parametrized using matrix Lie groups [21]. They utilize an Extended Kalman Filter on Lie Groups (LG-EKF) [22] and observed that their proposed framework improves estimation accuracy compared to the method based on Euler angle parametrization and EKF algorithm.

The global optimization-based estimation algorithm is usually used to encompass the more complex model definition and achieve higher estimation accuracy. In the work of M. Kok et al. [15], an optimization-based framework is proposed to solve the entire dataset offline using the infeasible start Gauss-Newton algorithm. A similar optimization framework is used in [16], where the optimization problem is solved based on factor graphs.

For methods using IMU orientation as the measurements in the system, a cascade of algorithms is needed for estimation. First of all, specific filters, like the Madgwick filter[23] and Mahony filter [24], are designed for estimating the orientation of IMUs. During this process, a magnetometer is usually used. Using the orientation estimated from these specific filters, the joint angle parametrized as Euler angles can be estimated using Inverse Kinematics (IK) which finds the joint angle that can track the IMU orientation [25] with minimum error. A well-established workflow for this method type has been proposed under the name OpenSense [26]. A similar IK algorithm can also be applied to the marker position measurements to achieve motion estimation [7].

The algorithm for estimating kinetics is called Inverse Dynamics (ID), which describes the process of estimating the kinetics based on the known inertial parameters of the system with the kinematics estimation [27]. Studies focused on kinematics estimation need an additional ID process to compute the kinetics. However, the work by D. Kanter [19] included a forward dynamics process in their model to achieve the estimation of kinematics and kinetics at the same time.

1-1-4   Benchmark Methods

How to evaluate a novel method for human motion estimation remains a subject of ongoing debate. In most of the studies, the marker-based sensing system is referred to as the gold standard which means the method serves as a benchmark, which is attainable under reasonable circumstances [28]. Although it may not be a flawless test, it represents the most reliable option with established outcomes. In a recent work by T. Uchida et al. [29], they propose that the most effective way to present marker-based estimation solutions is as a distribution of equally likely trajectories when accounting for sources of modeling uncertainty, such as marker alignment on the body and scaling of the model.

1-2   Motivation

Recently, D. Kanter's [19] has explored the use of IMUs as a sensing system and a kinetics model for analyzing robotic arm motion with EKF, which differs from previous methods that solely relied on kinematics for motion analysis. The initial results demonstrate promising accuracy; however, it is important to note that the robotic arm is fundamentally distinct from the human body. Therefore these differences identified by the author are provided here.

Differences in Anatomy Robotic arms and human arms have significant anatomical differences. The structure, range of motion, joint constraints, and motor control mechanisms in a robotic arm differ from those in a human arm. The robotic arm used in [19] only contains hinge joints while human joints are more flexible.

Dynamic and Real-World Factors Human motion is influenced by dynamic and real-world factors such as environmental interactions, motion in 3D spaces, and also Soft Tissue Artefacts (STA) [30]. Robotic arms typically operate in controlled environments with predetermined trajectories and limited external interactions. The absence of these dynamic factors in robotic systems can affect the validity and applicability of human motion estimation methods.

Unavailable Ground Truth The utilization of robotic arms as a means of validation provides ground truth data, enabling the optimization of hyperparameters and the evaluation process. Furthermore, robotic arms allow for accurate estimation of inertial parameters. However, this raises questions about the performance of the motion estimation method when human subjects are involved. The absence of ground truth data challenges the assessment of its efficacy [31], and accurately measuring the inertial parameters of human body segments is complex [32].

Given that experiments conducted on robotic arms do not encompass all the challenges posed by real human movements, it is currently no conclusion yet for the performance of applying a kinetics model for human motion estimation.

1-2-1   Research Question

The aforementioned problems motivate us to address the lack of conclusive evidence regarding the performance of the method using the kinetics model and IMU in human motion analysis, given the challenges of:

1. The model's higher complexity in joint mechanisms.

2. More abrupt and frequent changes in joint load on human subjects.

3. Highly dynamic motion that could potentially face STA.

To evaluate the performance, we will employ the marker-based IK/ID method as the benchmark. Furthermore, to gain insights into the characteristics of the method using the kinetics model, we will substitute the kinematics model for comparison. Additionally, we will make use of OpenSense for further comparison. These two comparisons will be conducted considering the following aspects, while still using the marker-based IK/ID method as the benchmark:

1. How does the estimation performance of the method using the kinetics model compare to the method using the kinematics model for human motion with IMU measurements?

2. What differences in model structure could lead to variations in estimation accuracy between methods based on kinetics and kinematics models?

1-2-2   Contribution

We have developed an 8 Degrees of Freedom (DoF) upper extremity model, simulating the right arm of the human body within OpenSim [33]. This model incorporates joint angles, velocities, and torques as state variables. For our estimation method, we've opted for the EKF, and we'll also test the IEKF to determine whether iterations in the EKF can enhance estimation accuracy.

To gauge the effectiveness of our proposed framework, we conducted experiments utilizing marker-based motion tracking and the IK/ID algorithms as baseline methods. These methods were selected due to their robustness in joint angle estimation. Additionally, we compared

our proposed framework with other approaches that employ IMUs and kinematics models. Detailed implementation information about our framework will be provided in subsequent chapters.

We employ representative wheelchair user motions to assess the versatility of our proposed framework. We have selected four distinct tasks, thoughtfully chosen to encompass a broad array of activities and scenarios involving highly dynamic wheelchair propulsion. This selection ensures the robustness and applicability of our proposed framework.

1-3   Thesis Outline

In Chapter 2, we present an overview of the relevant literature that inspired the current study.

Chapter 3 gives a description of the musculoskeletal model and the state space system used in our study.

The application of the EKF as our estimation algorithm and the rationale behind incorporating iterations to enhance estimation accuracy are presented in Chapter 4.

In Chapter 5, we present a detailed account of the marker and IMUs data that forms a vital part of our dataset. Additionally, we explain the calibration process for IMUs and outline the motion tasks and comparison methods employed in our study.

Chapter 6 showcases the outcomes of our experiments. Our conclusions, limitations, and suggestions for future research are detailed in Chapter 7.

Chapter 2

Related Work

Over the years, the development of IMU technology has undergone a remarkable transformation, evolving from large and bulky systems to compact, highly accurate, and energy-efficient devices. This significant progress has led to a surge in studies utilizing IMUs for human motion estimation. This chapter will focus on the existing studies of human motion estimation based on IMU. Even though the basis of our study is inspired by studies that explore the possibility of using kinetics for both kinematics and kinetics estimation, the contribution to the modeling and estimation strategy from the studies focusing on kinematics is also unneglectable. Therefore, we will first introduce some of the state-of-the-art methods based on kinematics for human motion estimation. And then we will introduce the existing works using kinetics for human motion estimation, which inspired our work.

2-1 Optimization-based Method Utilizing Quaternion Kinematics Model

For human motion estimation, each segment of the human body can be seen as an individual moving body. In the work of M. Kok et al. [15], the kinematics of the IMU is estimated by utilizing the IMU measurements signal, where the IMU is modeled using its position, velocity, and orientation as the states. Then, the IMU kinematics is related to the human body kinematics using the IMU alignment to the body. Since this alignment is assumed to be fixed, the position and orientation of the human body can be inferred when the IMU kinematics are known.

The orientation of each IMU was parameterized using quaternions, which belong to the 3-dimensional Lie group and provide a gimbal lock-free property compared to Euler angles [34]. The model's dynamics were established by integrating the accelerometer and gyroscope measurements from the IMU over time. Based on the integration of the accelerometer measurements, the rate of change of position and velocity can be obtained at each step. These rates are then integrated to predict the position and velocity of the IMU at the next time step. The

angular velocity measurements were integrated to predict the orientation of the IMU. However, the measurements from the IMU are noisy, and integration over time will unavoidably cause drift. Biomechanical characteristics are leveraged to correct the kinematics of the IMU, such as the common joints between the two body segments. Specifically, knowing the position and orientation of the human body enables us to express a vector of the human body frame *w.r.t.* the ground frame. For the vectors pointing to the joint centers from the two adjacent human body frames, these two vectors should be the same when expressed *w.r.t.* the ground frame. Another biomechanical characteristic used is that knee joints primarily work around one axis, and a term that penalizes rotation around axes other than the rotation axis of the hinge joint was formulated.

In the end, the optimization problem was formulated to minimize the error of IMU alignment, prediction of the dynamic model, hinge joint assumption, gyroscope bias prediction, initialization prediction, and zero mean acceleration assumption [35]. The characteristics of the common joint were used as the hard constraint. The IMU measurements are pre-collected, and the optimization problem is solved offline using the infeasible start Gauss-Newton method, which requires computing the Jacobian and approximating the Hessian. This work opens the gate of using IMU raw measurements for human motion estimation under the optimization framework and quaternion parametrization. The results show promising accuracy compared to marker-based sensing system estimated results.

2-2 Optimization-based Method Utilizing Rotation Matrix Kinematics Model

Another strategy, proposed in [36, 16], utilized rotation matrices to represent the orientation of the IMU and introduces an optimization problem with factor graphs as the computational framework. Factor graphs offer a powerful advantage for optimizing complex problems, efficiently representing the relationships between variables and constraints through a graphical model. This graphical representation enables the use of specialized message-passing algorithms, leading to faster convergence and scalability for large-scale optimization tasks [37]. Notably, in the work of T. Mcgrath et al. [36, 16], more anthropometry information was used as the state, including the limitations of segment length and width, biomechanical differences between the knee and femur length, and the angle between the hinge axis of the knee and the segments. This information, combined with a similar model as in [15], was solved within the factor graphs framework. The resulting accuracy for knee joint angle estimation was $3.47°$ and $5.21°$ for the right and left, respectively.

2-3 Nonlinear Kalman Filter-based Method Utilizing Quaternion Kinematics Model

In the work by I. Weygers et al. [14], a method similar to [15] was proposed to estimate the relative orientation between the IMUs attached to the human body flanking the same joint. Unlike [15], this method omits the hinge joints penalizing term, gyroscope measurements bias term, and zero mean acceleration assumption [35]. Instead of a common joint position, it leverages biomechanical characteristics of the common acceleration at the joint center.

In [14], the MEKF was employed to handle quaternion not residing in Euclidean space [14]. The MEKF uses a 3×3 noise covariance matrix for orientation parametrization, and the measurement update computes an orientation deviation represented by an angle-axis [20]. The MEKF only incorporates the dynamics of the IMU orientation in the prediction update, while the notion of common acceleration of the joint center with accelerometer measurements is utilized in the measurement update.

The study compared the estimation results obtained using MEKF to an optimization-based framework where only the error of initial estimation, dynamics of IMUs orientation, and measurements of the common joint acceleration were minimized. The optimization problem was solved using Gauss-Newton. Marker-based sensing estimation was used as the reference. The results demonstrated that although the absolute orientation estimation of the IMUs was drifting using MEKF under this framework, it was able to achieve non-drifting relative orientation between the IMUs flanking the joint. The optimization strategy achieved slightly higher estimation accuracy, and the MEKF took longer to converge at the initial condition.

2-4   Nonlinear Kalman Filter-based method Utilizing Euler Angle Kinematics Model

Although Euler angles have the problem of gimbal lock, they are still widely used in many biomechanical models [38, 39], including almost all models defined in OpenSim. This preference stems from their straightforward nature and ability to be assigned meaningful biomechanical definitions, such as flexion and adduction.

This modeling approach has been implemented in various studies [40, 12, 41, 11, 42]. Studies employing Euler angle parametrization often use the well-known Denavit–Hartenberg (DH) parametrization or the iterative velocity propagation modeling. The Euler angles are selected as a set of generalized coordinates to govern the state of the system. In these models, kinematic constraints are already embedded in the model, eliminating the need for extra constraints in the system. The generalized coordinates, velocity, and acceleration are used as the states with a constant acceleration model as its dynamics. The constant acceleration model involves a random walk model for the states of acceleration.

To estimate the model using Euler angles as states, the EKF has been utilized [40, 12], as Euler angles reside in Euclidean space. Unscented Kalman Filter (UKF) is also a viable substitute for the EKF [41, 11, 42], employing an unscented transform to approximate the nonlinear transform up to the third order.

2-5   Orientation-based Inverse Kinematics Utilizing Euler Angle

The method developed in [25] and [26] utilizes IMUs orientation and kinematic knowledge. The IMU measurements were combined with magnetometer measurements with a specific filter [23, 24] to get the orientation of the IMU. The IK is the process that minimizes the orientation difference between the output from the specific filter and the musculoskeletal model prediction for estimating the joint kinematics.

Karatsidis et al. [27] proposed a systematic workflow for estimating both the kinematics and the kinetics information using Anybody [43]. The OpenSense workflow proposed in [26] recommended taking the data pre-processing part, which eliminates the erroneous data that caused by ferromagnetic, to reproduce the experiment. Slade et al. [44] used a similar IK algorithm with the Mahony filter, but the RMSD shows drifting within 150 seconds.

2-6 Observability of the Kinematics Model

As observed in the study of [14], only the relative orientation between two IMUs was focused on, leading to non-drifting estimation results. However, there remains a risk of the system state becoming unobservable, as stated in the work of M. Kok et al. [17].

In [17], four different modeling strategies for human motion estimation were analyzed, all sharing a similar measurement model based on common joint position or common joint acceleration measurements. To assess the risk of unobservability, [17] employed the concept of differential observability [45] to determine under which circumstances the state cannot be uniquely determined by the measurements. By considering Wahba's problem [46], they found that the system becomes unobservable only when the specific force and the time derivative of acceleration at the center of the joint become linearly dependent. A metric was defined, averaging the norm of the cross-product of the specific force and the time derivative of acceleration over the past 100 steps. The results indicate that as this metric value is close to zero, uncertainty in the estimation results becomes large. Additionally, optimization-based estimation produced more accurate and certain results during unobservable durations compared to filter-based estimation.

In [36], observability was discussed without systematic proof. Two unobservable conditions related to the loss of heading were described. Firstly, the absolute position, velocity, and orientation of the human body are unobservable. Secondly, the hip joint, describing the relative orientation between the pelvis and thigh, becomes unobservable under conditions where the vectors of the common joint in the IMU frame are generally vertical or orthogonal to the heading plane, causing the IMU's orientation trajectory to become underconstrained, allowing multiple viable constant-offset heading solutions, particularly observed in upright walking gait with small step length. However, this condition does not apply to 1 DoF hinge joints, such as the knee joint, which are more constrained.

2-7 Optimal Motion Control for Motion Estimation

The optimal control methods proposed by E. Dorschky et al. [18] present a new approach to human motion estimation, incorporating the muscle force that controls the motion as part of the system's state. The estimation process in [18] is limited to an averaged gait cycle across all recorded datasets from IMU. The optimization problem's cost function aims to minimize differences between the actual IMU measurements and the simulated IMU signals from the optimal motion control model, averaged across all gait cycles. The method's constraints utilize the actual system dynamic model, where the states include muscle length and activation. Additionally, neural excitation of the muscle is considered as an input vector, while the

external forces, such as the ground reaction force, are modeled as part of the states, along with their contact points.

These methods attempt to incorporate more information, including muscle activations, to estimate the kinematics and kinetics of human motion. The work of [19] further simplifies the muscletendon system's complexity by focusing solely on the kinetics model, with joint torque included as part of the system's states, which will be elaborated on in the next section.

2-8   Kinetics Model with Euler Angle Parametrization

OpenSim is a biomechanical computational software based on SimBody, which is able to provide the kinetics of multibody systems [47]. In the work of D. Kanter [19], a robotic arm model was constructed within OpenSim, incorporating the forward dynamics equation of the system for human motion estimation. This approach includes joint torque as part of the system's states and facilitates the use of kinetics for both kinematics and kinetics estimation. The results show promising accuracy compared to the ground truth kinematics and kinetics provided by the robot encoder. D. Kanter also conducted a sensitivity test on IMU misalignment, finding that estimation accuracy is more affected by orientation misalignment than translation misalignment. Furthermore, the work has been extended by [31], where markers and IMUs measurements are fused for robot arm motion estimation. However, it's worth noting that this method has only been tested using robotic arms, which currently diminishes its applicability to human motion estimation, as challenges specific to human motion estimation have not been verified in the controlled environment of robotic arms. As shown in Table 2-1, most of the studies discussed in this chapter have been validated on human subjects, as the ultimate aim is for human motion estimation. Also, most of the works are focusing on using kinematics for human motion estimation.

The robotic arm used in the studies [19, 31] only has 1 DoF for each joint, which cannot be applied to the human body as the joint mechanism are more complex, e.g. the glenohumeral joint is a ball-and-socket joint. Also, the external force being applied to the robotic arm is smooth. In reality, humans can have more abrupt changes in the interaction force with the environment. Last, the body of the robotic arm is more rigid which almost has no STA involved. Therefore, the rationale of our study is to address the issue that the method proposed in [19] has not been validated when facing the challenges ubiquitous in human motion estimation.

Table 2-1: Summary of the studies of human motion estimation methods discussed in this chapter.

Study	Model	Estimation Method	Subject
[15]	Kinematics with quaternion	Optimization with nonfeasible start Gauss-Newton	human
[14]	Kinematics with quaternion	MEKF and Optimization with Gauss-Newton	human
[36]	Kinematics with rotation matrix	Optimization with factor graphs	human
[40, 12, 41, 42]	Kinematics with Euler angles	EKF,UKF	human
[25]	Kinematics with Euler angles	Inverse Kinematics	robotic arm
[26, 44, 27]	Kinematics with Euler angles	Inverse Kinematics	human
[18]	Kinetics model	Optimal control estimation	human
[11]	Kinematics with Euler angles	UKF	robotic arm
[19, 31]	Kinetics model	IEKF	robotic arm

Chapter 3

Modelling

In our study, we utilized OpenSim as the computational software to formulate the model of our system. The properties of the human body model, such as length and weight of the human body are defined in a `.osim` file that can be interpreted by OpenSim. Based on this defined model in OpenSim, the mathematical equation governing the motion of the human body can be constructed using OpenSim API in MATLAB. In this section, we will first introduce the convention of frame definition in OpenSim. After that, we will introduce the model definition in OpenSim for the upper extremity with the right arm of the human body. In the end, our state space model, which is based on the forward dynamics of the multibody system, will be elaborated.

3-1 Musculoskeletal Model Design

We adapted an existing OpenSim model proposed by Wu et al. [48] for our study. This model is scaled by the dataset supporter based on the approach also described by Wu et al. [48]. This allowed us to utilize pre-defined inertial parameters and segment lengths. While acknowledging the possibility of errors in these parameters, it should be noted that they remain consistent across all methods employed, ensuring a fair comparison.

To estimate the joint angle, usually, each segment of the human body is required to be attached 1 IMU. In our study, IMU has been placed on the thorax, humerus, and forearm. As the absolute position of the human body cannot be directly observed using only IMU measurements, we eliminated the translational DoF of the human body from our model. This refinement allows us to focus on the relevant joint motions while maintaining the integrity of the system. Furthermore, the complex shoulder joint definition in the original model can not be uniquely determined with the limited amount of IMU used in our study, the sternoclavicular and acromioclavicular joints are set as weld joints while retaining the DoF assigned to the glenohumeral joint. Therefore, we used the glenohumeral joint to represent the motion of the shoulder joint. Also, as no IMU has been placed on the hand, the wrist has been set as a weld joint. In the end, the original 17 DoF model is reduced to an 8 DoF model. The muscles

are excluded from our study. We will introduce the definition of the model in detail in the following section.

3-2 Frame Definition of OpenSim

Simbody is the primary library for OpenSim to create multi-body EoM. The fundamental unit of a multibody system is a rigid body associated with a joint that connects it to a parent body. This joint defines the coordinates and kinematic transformations that dictate the body's motion relative to its parent body. In Fig. 3-5, frame B and P are the joint coordinate frames fixed to the rigid body frame B_0 and P_0, respectively. They describe the kinematics relationship between the two moving body frames B_0 and P_0. In the following sections, we will refer to frames B and P as joint coordinate frames and B_0 and P_0 as body frames.
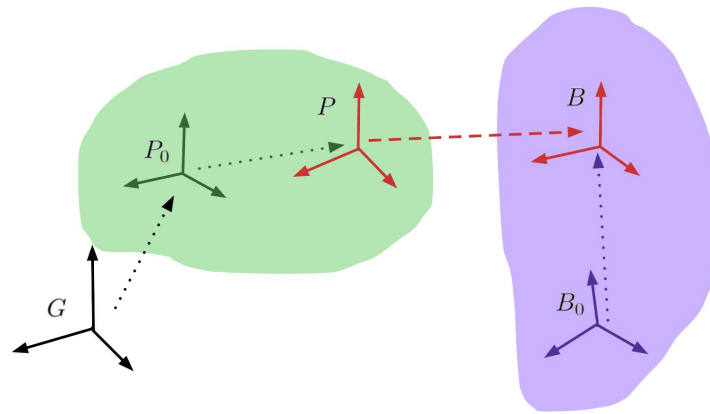
Figure 3-1: The convention of frame definition in OpenSim. Each frame has a body frame with a joint coordinate frame affixed. The joint coordinate frame is used to describe the kinematics relationship between the child body frame and the parent body frame.

3-3 Joints Definition

In this section, the definition of each joint is given using the screenshot of OpenSim GUI. The non-transparent body is rotated around one of the joint coordinates positively relative to the transparent body. To show the meaning of each joint, we will focus on the definition of the joint coordinates.

Joint Coordinates for the Thorax

In Fig. 3-2, the spine and the thorax in the model are the same rigid body and we will refer to this body as a whole using the name thorax. The joints coordinate of the thorax body is defined to be freely rotated *w.r.t.* the ground frame. It is a 3 DoF ball joint, with the joint coordinates: thorax list, thorax rotation, and thorax tilt illustrated in Fig. 3-2a, 3-2b, and 3-2c respectively. The joint coordinates on the thorax body have been defined closer to

(a) Thorax list(q_1)   **(b)** Thorax rot.(q_2)   **(c)** Thorax tilt(q_1)
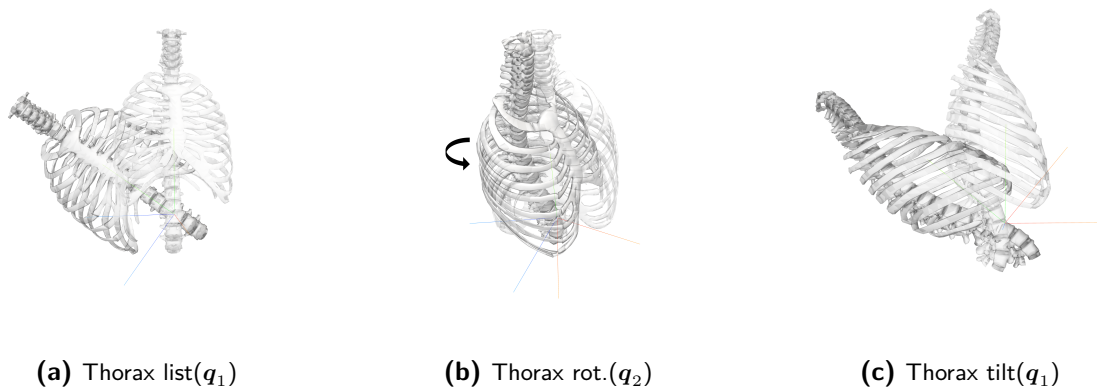
Figure 3-2: Three rotational joint coordinates define the kinematics relationship between the thorax body and the ground.

the sacrum on the spine to make the IMU specific force measurements effective. As the IMU has been placed closer to the sternum and the specific force measurements will be not effective for estimation if the origin of the joint coordinates frame is almost overlapped with the IMU frame. However, the definition of the position of this joint on the thorax remains debatable and could be further optimized.

Joint Coordinates for the Humerus and the Thorax

(a) Shoulder add.(q_4)   **(b)** Shoulder rot.(q_5)   **(c)** Shoulder flex.(q_6)
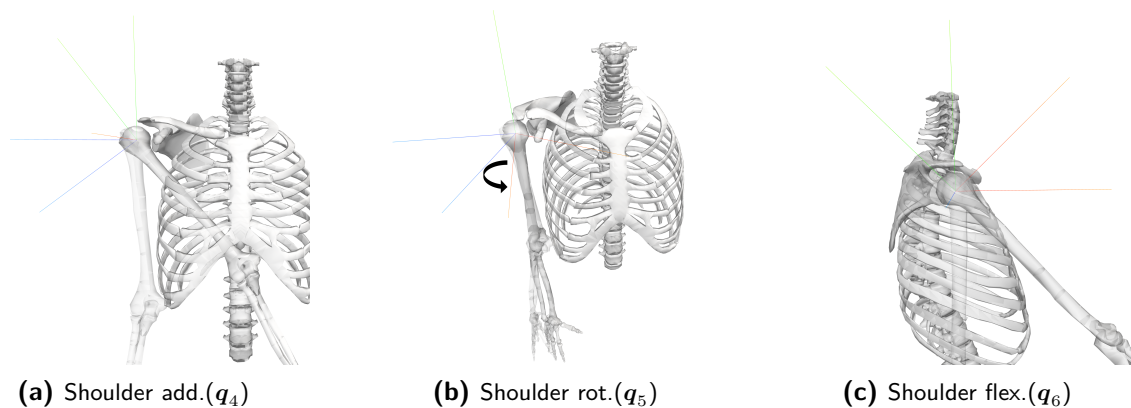
Figure 3-3: Three rotational joint coordinates define the kinematics relationship between the humerus body and the thorax body.

In Fig. 3-3, we demonstrate the definition of joint coordinates for the shoulder, which defines the kinematic relationship between the humerus body frame and the thorax body frame. As mentioned previously, the sternoclavicular and acromioclavicular are defined as weld joints. Also, the clavicle and scapula are fixed to the thorax and can be seen as the same rigid body. Therefore, in our model, the name shoulder or shoulder joint will actually only refer to the mechanism of the glenohumeral joint. The definition of three joint coordinates: shoulder adduction, shoulder rotation, and shoulder flexion are defined as in Fig. 3-3a, 3-3b, and 3-3c respectively. The positive direction of shoulder rotation is the direction of internal rotation.

Given the definition of the positive direction of rotation for shoulder adduction in Fig. 3-3a, we expect most of the tasks conducted by the human will be negative for the shoulder adduction joint.

Joint Coordinates for the Forearm

(a) Forearm flex.(q_7) **(b)** Forearm rot.(q_8)
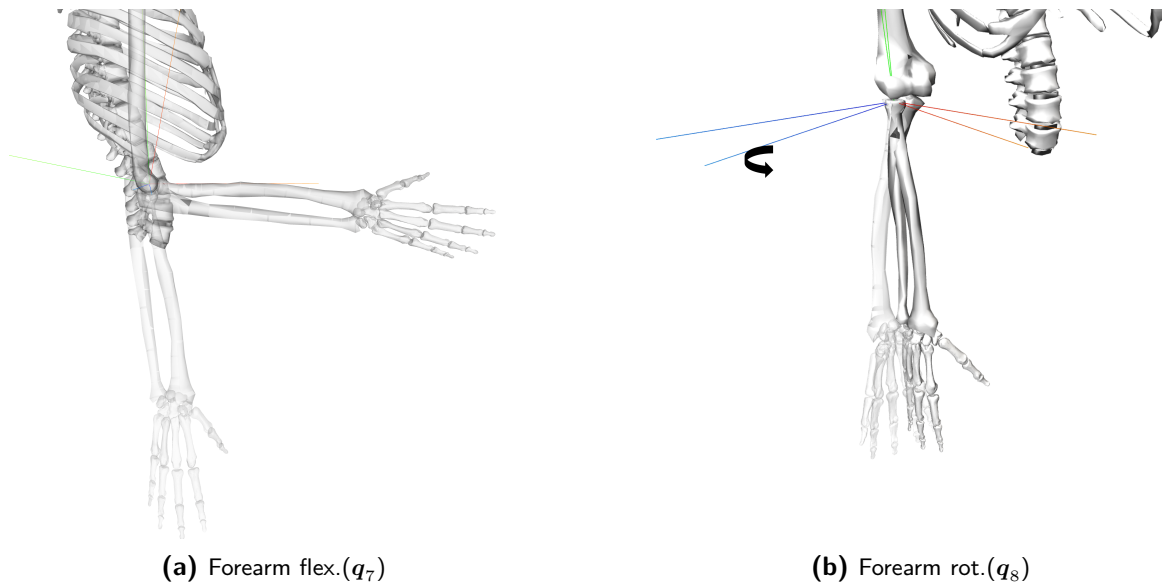
Figure 3-4: Two Joint coordinates define the kinematics of the forearm.

The forearm has two degrees of freedom: forearm flexion and forearm rotation. Fig. 3-4a shows the kinematics relationship between the ulna body frame of the forearm and the humerus body frame, while Fig. 3-4b shows the kinematics relationship between the radius body frame and the ulna body frame, with the positive direction of forearm rotation defined as pronation. The hand and radius are considered the same rigid body, and the wrist is defined as a weld joint due to the absence of an Inertial Measurement Unit (IMU) on the hand, which makes it impossible to estimate the movement of the hand.

Overview of the Joint Coordinates Definition

In our model, we use only the right arm's upper extremity, resulting in eight defined joint coordinates. These coordinates, thorax tilt, thorax list, thorax rotation, shoulder flexion, shoulder adduction, shoulder rotation, forearm flexion, and forearm rotation, each have one degree of freedom and are denoted as $q_1, q_2, \cdots, q_8$. The coordinates can freely rotate without range-of-motion constraints and are known as generalized coordinates. The model has seven rigid bodies: thorax, clavicle, scapula, humerus, ulna, radius, and hand. However, we consider relative motion between three rigid segments: the thorax (indexed as 1), the humerus (indexed as 2), and the forearm (indexed as 3), as shown in Fig. 3-5.

We have concluded the definition of our coordinate system in Table 3-1 with the definition and notation correspondence.
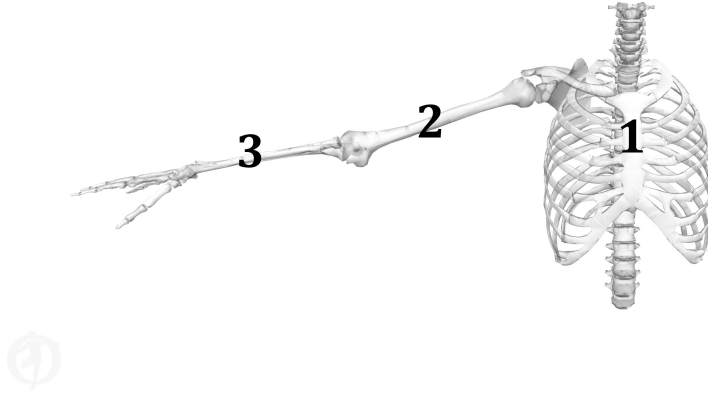
Figure 3-5: The overview of the model definition in OpenSim with an index on each body.

Table 3-1: Table of joints coordinates notation definition.

Joint Name	Notation
Thorax tilt	q_1
Thorax list	q_2
Thorax rotation	q_3
Shoulder flexion	q_4
Shoulder adduction	q_5
Shoulder rotation	q_6
Forearm flexion	q_7
Forearm rotation	q_8

3-4   Sensor Models

Before we use the forward dynamics to construct the state space model of our system, we will introduce the measurements model of sensors used in our study. To be able to capture accurate kinetics knowledge, we need to know the external force applied to the human body. Therefore, the measurements of the force sensor will be introduced. On the other hand, to gain kinematics knowledge of the movements of the human body, IMUs are the sensors we used to capture kinematics signals.

3-4-1   Force Sensor

From our dataset at hand, the force measurements have already been transferred to be expressed in the ground frame in OpenSim. We assume the force measurements are accompanied by a zero mean white noise v_f and the measurements model is given as

$$u = f_{\text{ext}} + v_f \quad v_f \sim \mathcal{N}\left(0, Q_f\right), \tag{3-1}$$

where f_{ext} is the actual external force, u is the force measurements.

3-4-2   IMUs Measurement Model

An IMU comprises an accelerometer and a gyroscope, which measure the specific force and angular velocity, respectively. The frame of the IMU is represented by s_i, where i indicates the index of the body frame to which it is attached, as indicated in Fig. 3-5. These measurements are expressed in the sensor frame and can be described by

$$^{s_i}y_{\mathrm{a}} = {}^{s_i}\mathrm{a}_{s_i} - {}^{s_i}g + \boldsymbol{e}_{s_i,\mathrm{a}} \quad \boldsymbol{e}_{s_i,\mathrm{a}} \sim \mathcal{N}\left(0, R_{s_i,\mathrm{a}}\right) \tag{3-2a}$$

$$^{s_i}y_{\omega} = {}^{s_i}\omega_{s_i} + \boldsymbol{e}_{s_i,\omega} \quad \boldsymbol{e}_{s_i,\omega} \sim \mathcal{N}\left(0, R_{s_i,\omega}\right), \tag{3-2b}$$

where $^{s_i}y_{\mathrm{a}}$ is the specific force measurements, $^{s_i}y_{\omega}$ is the angular velocity measurements, $^{s_i}\mathrm{a}_{s_i}$ is the acceleration, ^{s_i}g is the gravity force, and $^{s_i}\omega_{s_i}$ is the angular velocity, which are all measured $w.r.t.$ IMU frame s_i. $\boldsymbol{e}_{s_i,\mathrm{a}}$ and $\boldsymbol{e}_{s_i,\omega}$ are the Gaussian noise term related to accelerometer measurement and gyroscope measurement respectively.

3-5   Forward Dynamics

Forward dynamics is a mathematical model that governs the changes in joint coordinates and their velocities resulting from applied forces and torques. OpenSim is capable of solving the forward dynamics based on the model defined in the previous section as specified in OpenSim user's guide [49]

$$\ddot{\boldsymbol{q}} = \mathbf{M}(\boldsymbol{q})^{-1}\left(\boldsymbol{\tau} + C(\boldsymbol{q}, \dot{\boldsymbol{q}}) + \bar{\mathbf{Q}} + \mathbf{Q}\right), \tag{3-3}$$

where $\boldsymbol{q} = [\boldsymbol{q}_1, \cdots, \boldsymbol{q}_8]^{\top}$, $\ddot{\boldsymbol{q}}$ is the joint acceleration casued by joint torques $\boldsymbol{\tau} = [\boldsymbol{\tau}_1, \cdots, \boldsymbol{\tau}_8]^{\top}$, applied forces $\mathbf{Q}$, gravity induced forces $\bar{\mathbf{Q}}$, and Coriolis and centrifugal forces $C(\boldsymbol{q}, \dot{\boldsymbol{q}})$. $\mathbf{M}(\boldsymbol{q})^{-1}$ is the generalized mass matrix. Eq. (3-3) will be used and calculated from OpenSim.

Note that the $\mathbf{Q}$ are defined in the generalized space, while the external force we measured as in Eq. (3-1) are expressed in the Cartesian space. To map the force we know in the Cartesian space to the generalized space, we will leverage the point Jacobian of the system [50]. For an arbitrary point located at one of the bodies in our model, e.g. the external force applied point denoted by $\dot{p}_f$, we could use

$$\dot{p}_f = J_f \dot{\boldsymbol{q}}, \tag{3-4}$$

to define the relationship between the velocity of a point on the model in Cartesian space and the velocity of generalized coordinates, where $\dot{p}_f$ is the linear velocity at the external force applied point p_f and J_f is the point Jacobian. The transpose of the point Jacobian could map the applied force on the body in Cartesian space to generalized space [50]. Therefore, we substitute $\mathbf{Q}$ using equation

$$\mathbf{Q} = J_f^{\top} f_{\mathrm{ext}} = J_f^{\top}\left(u + v_f\right), \tag{3-5}$$

where the sign for the noise term is flipped without loss of generality.

3-6   State Space Model

To incorporate the forward dynamics into our state space model, the state of our system is chosen to be the generalized coordinates, generalized velocities, and the generalized torque, namely $\boldsymbol{q}$, $\dot{\boldsymbol{q}}$, and $\boldsymbol{\tau}$. The state $\boldsymbol{x}$ is defined as

$$\boldsymbol{x} = \begin{bmatrix} \boldsymbol{q} \\ \dot{\boldsymbol{q}} \\ \boldsymbol{\tau} \end{bmatrix}. \tag{3-6}$$

Substituting $\mathbf{Q}$ using Eq. (3-5) in the forward dynamics Eq. (3-3), our state sapce model is defined as

$$\dot{\boldsymbol{x}}(t) = \begin{bmatrix} \dot{\boldsymbol{q}} \\ \ddot{\boldsymbol{q}} \\ \dot{\boldsymbol{\tau}} \end{bmatrix} = \begin{bmatrix} \dot{\boldsymbol{q}} \\ \mathbf{M}(\boldsymbol{q})^{-1}(J_f^\top u + \boldsymbol{\tau} + \bar{\mathbf{Q}} + \mathbf{C}(\boldsymbol{q},\dot{\boldsymbol{q}})) \\ \mathbf{0} \end{bmatrix} + \begin{bmatrix} v_q \\ \mathbf{M}(\boldsymbol{q})^{-1}J_f^\top v_f \\ v_{\boldsymbol{\tau}} \end{bmatrix} = \bar{f}(\boldsymbol{x}, u, \boldsymbol{v}), \tag{3-7}$$

where the noise term of the system is defined as

$$\boldsymbol{v} \sim \mathcal{N}(0, Q), \quad \boldsymbol{v} = \begin{bmatrix} v_q \\ v_f \\ v_{\boldsymbol{\tau}} \end{bmatrix}, \quad Q = \begin{bmatrix} Q_q & \mathbf{0} & \mathbf{0} \\ \mathbf{0} & Q_f & \mathbf{0} \\ \mathbf{0} & \mathbf{0} & Q_{\boldsymbol{\tau}} \end{bmatrix}, \tag{3-8}$$

$Q_{\boldsymbol{q}}$, Q_f, and $Q_{\boldsymbol{\tau}}$ are matrices with noise covariance of each state on the diagonal.

3-7   Measurement Model

Assuming that the IMU is rigidly attached to the body segments, we can determine the point Jacobian that maps the generalized coordinates to the linear and angular velocity at the center of the IMU frame with

$$\begin{bmatrix} {}^{s_i}v_{s_i} \\ {}^{s_i}\omega_{s_i} \end{bmatrix} = \begin{bmatrix} {}^{s_i}J_{s_i,v} \\ {}^{s_i}J_{s_i,\omega} \end{bmatrix} \dot{\boldsymbol{q}} = {}^{s_i}J_{s_i}\dot{\boldsymbol{q}}, \tag{3-9}$$

Where ${}^{s_i}v_{s_i}$ and ${}^{s_i}\omega_{s_i}$ represent the linear and angular velocity at the origin of IMU frame s_i, respectively, expressed in the IMU frame. The point Jacobian of s_i IMU frame, denoted as ${}^{s_i}J_{s_i}$, comprises the linear velocity Jacobian ${}^{s_i}J_{s_i,v}$ and the angular velocity Jacobian ${}^{s_i}J_{s_i,\omega}$, which are all expressed in IMUs frame. To compute the acceleration at the origin of the IMU frame, we take the time derivative of ${}^{s_i}v_{s_i}$

$$^{s_i}\mathrm{a}_{s_i} = {}^{s_i}J_{s_i,v}\ddot{\boldsymbol{q}} + {}^{s_i}\dot{J}_{s_i,v}\dot{\boldsymbol{q}}, \tag{3-10}$$

where ${}^{s_i}\mathrm{a}_{s_i} = {}^{s_i}\dot{v}_{s_i}$.

Combining Eq. (3-10) with IMUs measurements model given in Eq. (3-2), we will have

$$
\begin{aligned}
{}^{s_i}y_{\mathrm{a}} &= {}^{s_i}J_{s_i,v}\ddot{\boldsymbol{q}} + {}^{s_i}\dot{J}_{s_i,v}\dot{\boldsymbol{q}} - {}^{s_i}g + \boldsymbol{e}_{s_i,\mathrm{a}} \quad \boldsymbol{e}_{s_i,\mathrm{a}} \sim \mathcal{N}\left(0, R_{s_i,\mathrm{a}}\right) &\text{(3-11a)}\\
{}^{s_i}y_{\omega} &= {}^{s_i}J_{s_i,\omega}\dot{\boldsymbol{q}} + \boldsymbol{e}_{s_i,\omega} \quad \boldsymbol{e}_{s_i,\omega} \sim \mathcal{N}\left(0, R_{s_i,\omega}\right). &\text{(3-11b)}
\end{aligned}
$$

Substituting Eq. (3-3) with force measurements being mapped onto generalized space and v_f into Eq. (3-11), the final measurements model is defined as

$$
y = \begin{bmatrix} \vdots \\ {}^{s_i}y_{\mathrm{a}} \\ {}^{s_i}y_{\omega} \\ \vdots \end{bmatrix} = \begin{bmatrix} \vdots \\ {}^{s_i}J_{s_i,v}\mathbf{M}(\boldsymbol{q})^{-1}(J_f^\top u + \boldsymbol{\tau} + \bar{\mathbf{Q}} + \mathbf{C}(\boldsymbol{q},\dot{\boldsymbol{q}}) + J_f^\top v_f) + {}^{s_i}\dot{J}_{s_i,v}\dot{\boldsymbol{q}} - {}^{s_i}g + \boldsymbol{e}_{s_i,\mathrm{a}} \\ {}^{s_i}J_{s_i,\omega}\dot{\boldsymbol{q}} + \boldsymbol{e}_{s_i,\omega} \\ \vdots \end{bmatrix},
$$

$$\text{(3-12)}$$

where $i = 1, 2, 3$. The equation constituting all the measurements with the time k to represent the measurement time step is defined as

$$
y_k = h\left(\boldsymbol{x}_k, u_k, v_f, \boldsymbol{e}\right),
$$

$$\text{(3-13)}$$

where

$$
v_f \sim \mathcal{N}\left(0, Q_f\right),
$$

$$
\boldsymbol{e} \sim \mathcal{N}\left(0, R\right), \quad \boldsymbol{e} = \begin{bmatrix} \boldsymbol{e}_{s_1,\mathrm{a}} \\ \boldsymbol{e}_{s_1,\omega} \\ \boldsymbol{e}_{s_2,\mathrm{a}} \\ \boldsymbol{e}_{s_2,\omega} \\ \boldsymbol{e}_{s_3,\mathrm{a}} \\ \boldsymbol{e}_{s_3,\omega} \end{bmatrix}, \quad R = \mathrm{diagonal}([R_{s_1,\mathrm{a}}, R_{s_1,\omega}, R_{s_2,\mathrm{a}}, R_{s_2,\omega}, R_{s_3,\mathrm{a}}, R_{s_3,\omega}]).
$$

Chapter 4

Methods

In this chapter, we will specify the EKF and IEKF used for state estimation. IEKF leverages the nature of EKF as a solver for nonlinear least square problems using the Gauss-Newton algorithm, which can be solved iteratively. EKF takes the first-order approximation of the nonlinear system, while a single iteration could make it far from the optimal value. IEKF is a possible alternate to solve this issue. This section follows the derivation provided in [51].

4-1 The EKF and IEKF Algorithms

EKF and IEKF can be interchanged easily, as only conducting the first iteration in IEKF is the EKF algorithm. Since the EKF produces estimates that are equivalent to the expectation of the underlying Gaussian distribution, we will adopt the following notation

$$
\begin{aligned}
\hat{\boldsymbol{x}}_{k|k} &= \mathbb{E}\left[\boldsymbol{x}_k \mid Y_k\right], & \hat{\boldsymbol{x}}_{k|k-1} &= \mathbb{E}\left[\boldsymbol{x}_k \mid Y_{k-1}\right], \\
P_{k|k} &= \mathrm{Cov}\left(\boldsymbol{x}_k \mid Y_k\right), \text{and} & P_{k|k-1} &= \mathrm{Cov}\left(\boldsymbol{x}_k \mid Y_{k-1}\right),
\end{aligned}
\tag{4-1}
$$

where $\mathbb{E}\left[\boldsymbol{x}_k \mid Y_k\right]$ and $\mathrm{Cov}\left(\boldsymbol{x}_k \mid Y_k\right)$ represents taking the expectation and covariance of x_k depends on all the past measurements $Y_k = (y_0, \ldots, y_k)$.

4-1-1   Prediction

The Runge-Kutta fourth-order algorithm is used to compute the $\boldsymbol{x}_{k+1}$ based on $\boldsymbol{x}_k$ using the following equation

$$
\begin{aligned}
l_1 &= \bar{f}\left(\boldsymbol{x}_k, u_k, 0\right), \\
l_2 &= \bar{f}\left(\boldsymbol{x}_k + T\frac{l_1}{2}, u_k, 0\right), \\
l_3 &= \bar{f}\left(\boldsymbol{x}_k + T\frac{l_2}{2}, u_k, 0\right), \\
l_4 &= \bar{f}\left(\boldsymbol{x}_k + Tl_3, u_k, 0\right), \\
\boldsymbol{x}_{k+1} &= \boldsymbol{x}_k + \frac{\bar{f}\left(l_1 + 2l_2 + 2l_3 + l_4\right)}{6} = f\left(\boldsymbol{x}_k, u_k, 0\right).
\end{aligned}
\tag{4-2}
$$

Therefore, we have the prediction of the system as

$$
\begin{aligned}
\mathbb{E}\left[\boldsymbol{x}_{k+1} \mid Y_k\right] &= \mathbb{E}\left[f\left(\boldsymbol{x}_k, u_k, v_k\right) \mid Y_k\right], \\
\hat{\boldsymbol{x}}_{k+1|k} &= f(\hat{\boldsymbol{x}}_{k|k}, u_k, 0),
\end{aligned}
\tag{4-3}
$$

where $\hat{\boldsymbol{x}}_{k|k}$ is the estimation result from the previous step.

Discretization

To update the predication of the covariance matrix, we need the discrete system matrices. As the discretization strategy we used relies on linear dynamics model [52], we will begin by linearizing the state-space model at the current operating point $\boldsymbol{x}_k = [\boldsymbol{q}_k, \dot{\boldsymbol{q}}_k, \boldsymbol{\tau}_k]^\top$ by calculating its approximation by first order Tyler expansion

$$
\dot{\boldsymbol{x}} = \bar{f}\left(\boldsymbol{x}, u, \boldsymbol{v}\right) \approx \bar{f}\left(\boldsymbol{x}_k, u_k, \boldsymbol{v}\right) + A_{\boldsymbol{x}_k}\left(\boldsymbol{x} - \boldsymbol{x}_k\right) + B_{u, \boldsymbol{x}_k} u_k + B_{\boldsymbol{v}, \boldsymbol{x}_k} \boldsymbol{v}.
\tag{4-4}
$$

Following the computation strategy for the Jacobian matrix in J. Boelens work [31], we have

$$
\begin{aligned}
A_{\boldsymbol{x}_k} &= \left.\frac{\partial \bar{f}\left(\boldsymbol{x}, u, \boldsymbol{v}\right)}{\partial \boldsymbol{x}}\right|_{\substack{\boldsymbol{x}=\boldsymbol{x}_k \\ u=u_k \\ v=0}} = \begin{bmatrix} \boldsymbol{0} & I_{N_q} & \boldsymbol{0} \\ \frac{\partial \ddot{\boldsymbol{q}}_k}{\partial \boldsymbol{q}_k} & \frac{\partial \ddot{\boldsymbol{q}}_k}{\partial \dot{\boldsymbol{q}}_k} & \mathbf{M}(\boldsymbol{q}_k)^{-1} \\ \boldsymbol{0} & \boldsymbol{0} & \boldsymbol{0} \end{bmatrix} \\[2mm]
B_{u, \boldsymbol{x}_k} &= \left.\frac{\partial \bar{f}\left(\boldsymbol{x}, u, \boldsymbol{v}\right)}{\partial u}\right|_{\substack{\boldsymbol{x}=\boldsymbol{x}_k \\ u=u_k \\ v=0}} = \begin{bmatrix} \boldsymbol{0} \\ \mathbf{M}(\boldsymbol{q}_k)^{-1} J_f^\top \\ \boldsymbol{0} \end{bmatrix} \\[2mm]
B_{\boldsymbol{v}, \boldsymbol{x}_k} &= \left.\frac{\partial \bar{f}\left(\boldsymbol{x}, u, \boldsymbol{v}\right)}{\partial \boldsymbol{v}}\right|_{\substack{\boldsymbol{x}=\boldsymbol{x}_k \\ u=u_k}} = \begin{bmatrix} I_{N_q} & \boldsymbol{0} & \boldsymbol{0} \\ \boldsymbol{0} & \mathbf{M}(\boldsymbol{q}_k)^{-1} J_f^\top & \boldsymbol{0} \\ \boldsymbol{0} & \boldsymbol{0} & I_{N_q} \end{bmatrix}.
\end{aligned}
\tag{4-5}
$$

In Eq. (4-5), $\frac{\partial \ddot{\boldsymbol{q}}_k}{\partial \boldsymbol{q}_k}$ and $\frac{\partial \ddot{\boldsymbol{q}}_k}{\partial \dot{\boldsymbol{q}}_k}$ need to be computed based on the forward dynamics function as introduced in Eq. (3-3), which can be returned by Simbody function `calcAcceleration`.

I_{N_q} is the identity matrix with a dimension of the number generalized coordinates N_q. The inverse of the generalized mass matrix $\mathbf{M}(\boldsymbol{q}_k)^{-1}$ can be returned by OpenSim API function `calcMInv`. J_f is the Jacobian of the point where the external force is applied, which can be computed using `calcStationJacobian`.

Eq. (4-4) is reorganized for discretization as

$$\dot{\boldsymbol{x}} \approx A_{\boldsymbol{x}_k}\boldsymbol{x} + B_{u,\boldsymbol{x}_k}u_k + B_{\boldsymbol{v},\boldsymbol{x}_k}\boldsymbol{v} + \underbrace{\bar{f}\left(\boldsymbol{x}_k, u_k, \boldsymbol{v}\right) + A_{\boldsymbol{x}_k}\boldsymbol{x}_k}_{f_{const}}.$$

(4-6)

Using Eq. (4-6), the discrete model can be derived using the following formula from [52]. The matrix for discrete time system model $F_{\boldsymbol{x}_k}$, $L_{u,\boldsymbol{x}_k}$, and $L_{\boldsymbol{v},\boldsymbol{x}_k}$ is given by

$$e^{\begin{bmatrix} A_{\boldsymbol{x}_k} & B_{u,\boldsymbol{x}_k} & B_{\boldsymbol{v},\boldsymbol{x}_k} & f_{const} \\ \mathbf{0} & \mathbf{0} & \mathbf{0} & \mathbf{0} \end{bmatrix} \cdot T} = \begin{bmatrix} F_{\boldsymbol{x}_k} & L_{u,\boldsymbol{x}_k} & L_{\boldsymbol{v},\boldsymbol{x}_k} & \bar{f}_{const} \\ \mathbf{0} & \mathbf{I} & \mathbf{I} & \mathbf{I,} \end{bmatrix}$$

(4-7)

where T denotes the sampling time of the system, $\mathbf{0}$ on the left-hand side of the equation is of the size to make the matrix a square matrix, which is the same for the $\mathbf{0}$ and $\mathbf{I}$ on the right-hand side. Using Eq. (4-7), we have computed the discretized matrices of discrete system matrix $F_{\boldsymbol{x}_k}$, discrete input matrix $L_{u,\boldsymbol{x}_k}$, and discrete noise matrix $L_{\boldsymbol{v},\boldsymbol{x}_k}$.

The corresponding covariance matrix of the prediction is found based on the discretized system

$$\begin{aligned} P_{k+1|k} &= \mathbb{E}\left[\left(\boldsymbol{x}_{k+1} - \hat{\boldsymbol{x}}_{k+1|k}\right)\left(\boldsymbol{x}_{k+1} - \hat{\boldsymbol{x}}_{k+1|k}\right)^{\top}\right] \\ &= F_{\hat{\boldsymbol{x}}_{k|k}}P_{k|k}F_{\hat{\boldsymbol{x}}_{k|k}}^{\top} + L_{\boldsymbol{v},\hat{\boldsymbol{x}}_{k|k}}QL_{\boldsymbol{v},\hat{\boldsymbol{x}}_{k|k}}^{\top}. \end{aligned}$$

(4-8)

4-1-2   Correction

Based on the prediction step, this section focuses on solving the EKF from the viewpoint of the nonlinear least square problem using Gauss-Newton algorithm. We will start with Bayesian inference based on the value from the prediction and measurements. If we expand the equation for Bayesian inference, we will find that it is equivalent to a nonlinear least square formulation [51]. The noise covariance matrix Q and R comes into play and can be interpreted as the weights in the nonlinear least square problem, where the process noise $\boldsymbol{v}$ and measurements noise $\boldsymbol{e}$ are assumed to be uncorrelated. The iterative nature of the Gauss-Newton solver enables us to iteratively solve EKF, which formulates the IEKF. In the following derivation, the time step is shifted backward for one step for simplicity without loss of generality.

First of all, from Bayesian inference [53], we have

$$p\left(\boldsymbol{x}_k \mid Y_k\right) \propto p\left(y_k \mid \boldsymbol{x}_k\right) p\left(\boldsymbol{x}_k \mid Y_{k-1}\right).$$

(4-9)

Based on the prediction step, we have the distribution of the prediction as

$$p\left(\boldsymbol{x}_k \mid Y_{k-1}\right) \sim \mathcal{N}\left(\hat{\boldsymbol{x}}_{k|k-1}, P_{k|k-1}\right).$$

(4-10)

We linearize our measurement model at an operating point $\boldsymbol{x}_{op,k}$ near current state $\boldsymbol{x}_k$ at step k as

$$y_k = h\left(\boldsymbol{x}_k, u_k, v_f, \boldsymbol{e}\right) \approx y_{\boldsymbol{x}_{op,k}} + H_{\boldsymbol{x}_{op,k}}\left(\boldsymbol{x}_k - \boldsymbol{x}_{op,k}\right) + D_{\boldsymbol{x}_{op,k}} v_f + M_{\boldsymbol{x}_{op,k}} \boldsymbol{e}$$

$$H_{\boldsymbol{x}_{op,k}} = \left.\frac{\partial h\left(\boldsymbol{x}_k, u_k, v_f, \boldsymbol{w}_k\right)}{\partial \boldsymbol{x}_k}\right|_{\substack{\boldsymbol{x}_k=\boldsymbol{x}_{op,k} \\ u_k=u_k \\ v_f=0 \\ \boldsymbol{e}=0}} \qquad M_{\boldsymbol{x}_{op,k}} = \left.\frac{\partial h}{\partial \boldsymbol{e}}\right|_{\substack{\boldsymbol{x}_k=\boldsymbol{x}_{op,k} \\ u_k=u_k}} = \mathbf{I}_{Ny}$$

$$D_{\boldsymbol{x}_{op,k}} = \left.\frac{\partial h\left(\boldsymbol{x}_k, u_k, v_f, \boldsymbol{e}\right)}{\partial v_f}\right|_{\substack{\boldsymbol{x}_k=\boldsymbol{x}_{op,k} \\ u_k=u_k}} \qquad y_{\boldsymbol{x}_{op,k}} = h(\boldsymbol{x}_{op,k}, u_k, 0, 0), \tag{4-11}$$

where N_y represents the number of measurements at each time step, $\mathbf{I}_{Ny}$ denotes the N_y-dimensional identity matrix, v_f is the process noise term left over in the measurement model as the input signal also comes into play in the measurements model. If we take $\boldsymbol{x}_k = \boldsymbol{x}_{op,k}$, we will have

$$y_k \approx h\left(\boldsymbol{x}_k, u_k, 0, 0\right) + D_{\boldsymbol{x}_k}\bar{\boldsymbol{v}}_k + M_{\boldsymbol{x}_k}\boldsymbol{\omega}_k. \tag{4-12}$$

Taking the expectation on both sides, the above equation becomes

$$P\left(y_k \mid \boldsymbol{x}_k\right) \sim \mathcal{N}(h\left(\boldsymbol{x}_k\right), \underbrace{D_{\boldsymbol{x}_k}Q_f D_{\boldsymbol{x}_k}^\top + M_{\boldsymbol{x}_k}R M_{\boldsymbol{x}_k}^\top}_{\bar{R}}), \tag{4-13}$$

where the $h\left(\boldsymbol{x}_k, u_k, 0, 0\right)$ has been simplified to $h\left(\boldsymbol{x}_k\right)$ as u_k will be constant in each time instance. Q_f represents the covariance of the input noise. Substituting Eq. (4-10) and (4-13) into Eq. (4-9), we could write out the mathematical expression for Gaussian distribution. By taking the negative logarithm and removing the constant coefficient, we have

$$\hat{\boldsymbol{x}}_{k|k} = \arg\min_{x_k} L(\boldsymbol{x}_k), \tag{4-14a}$$

$$L(\boldsymbol{x}_k) = \frac{1}{2}(Z - g(\boldsymbol{x}_k))^\top \bar{Q}^{-1}(Z - g(\boldsymbol{x}_k)), \tag{4-14b}$$

as our cost function with the definition

$$Z = \begin{bmatrix} y_k \\ \hat{\boldsymbol{x}}_{k|k-1} \end{bmatrix}, \quad Z \sim \mathcal{N}\left[\begin{pmatrix} h(\boldsymbol{x}_k) \\ \boldsymbol{x}_k \end{pmatrix}, \bar{Q}\right],$$

$$g(\boldsymbol{x}_k) = \begin{bmatrix} h(\boldsymbol{x}_k) \\ \boldsymbol{x}_k \end{bmatrix}, \quad \bar{Q} = \begin{bmatrix} \bar{R} & 0 \\ 0 & P_{k|k-1} \end{bmatrix}, \tag{4-15}$$

where $\bar{Q}$ represents the covariance and should be positive semi-definite. We find Eq. (4-14b) is a least square problem and we assigned S, $r\left(\boldsymbol{x}_k\right)$, and $G_{\boldsymbol{x}_k}$ as

$$S^\top S = \bar{Q}^{-1}, \quad r\left(\boldsymbol{x}_k\right) = S \cdot \left(Z - g\left(\boldsymbol{x}_k\right)\right), \quad G_{\boldsymbol{x}_k} = \begin{bmatrix} H_{\boldsymbol{x}_k} \\ I_n \end{bmatrix}, \tag{4-16}$$

where $G_{\boldsymbol{x}_k}$ is the time derivative of $g(\boldsymbol{x}_k)$. The derivative for $L(\boldsymbol{x}_k)$ is defined as [54]

$$\begin{aligned}
\nabla L(\boldsymbol{x}_k) &= \dot{r}(\boldsymbol{x}_k)^\top r\left(\boldsymbol{x}_k\right) \\
\nabla L(\boldsymbol{x}_k) &= -G_{\boldsymbol{x}_k}^\top S^\top S(Z - g(\boldsymbol{x}_k)) \\
&= -G_{\boldsymbol{x}_k}^\top \bar{Q}^{-1}(Z - g(\boldsymbol{x}_k)),
\end{aligned} \tag{4-17}$$

For the Hessian matrix of Eq. (4-14b), we used the following approximation as given in [54]

$$\begin{aligned}
\nabla^2 L(\boldsymbol{x}_k) &\approx \dot{r}(\boldsymbol{x}_k)^\top \dot{r}(\boldsymbol{x}_k) \\
\nabla^2 L(\boldsymbol{x}_k) &\approx G_{\boldsymbol{x}_k}^\top S^\top S G_{\boldsymbol{x}_k} \\
&\approx G_{\boldsymbol{x}_k}^\top \bar{Q}^{-1} G_{\boldsymbol{x}_k}.
\end{aligned} \tag{4-18}$$

Utilizing the Gauss-Newton algorithm [51], we are able to solve the cost function in Eq. (4-14b)

$$\boldsymbol{x}_{k,i+1} = \boldsymbol{x}_{k,i} - \left(\nabla^2 L\left(\boldsymbol{x}_{k,i}\right)\right)^{-1} \nabla L\left(\boldsymbol{x}_{k,i}\right) \tag{4-19a}$$

$$= \boldsymbol{x}_{k,i} + \left(G_{\boldsymbol{x}_{k,i}}^\top \bar{Q}^{-1} G_{\boldsymbol{x}_{k,i}}\right)^{-1} G_{\boldsymbol{x}_{k,i}}^\top \bar{Q}^{-1} \left(Z - g\left(\boldsymbol{x}_{k,i}\right)\right) \tag{4-19b}$$

$$= \left(G_{\boldsymbol{x}_{k,i}}^\top \bar{Q}^{-1} G_{\boldsymbol{x}_{k,i}}\right)^{-1} G_{\boldsymbol{x}_{k,i}}^\top \bar{Q}^{-1} \left(Z - g\left(\boldsymbol{x}_{k,i}\right) + G_{\boldsymbol{x}_{k,i}} \boldsymbol{x}_{k,i}\right). \tag{4-19c}$$

The right subscription i is used to denote the iteration step at time instance k. $G_{\boldsymbol{x}_{k,i}}$ is also needed to be recomputed in each iteration. As we can see, during the iteration of Gauss-Newton, the Hessian matrix $G_{\boldsymbol{x}_{k,i}}^\top \bar{Q}^{-1} G_{\boldsymbol{x}_{k,i}}$ is also computed repeatedly.

If we expand Eq. (4-19c), we will find the following equation

$$\boldsymbol{x}_{k,i+1} = \hat{\boldsymbol{x}}_{k|k-1} + \left(H_{\boldsymbol{x}_{k,i}}^\top R^{-1} H_{\boldsymbol{x}_{k,i}} + P_{k|k-1}^{-1}\right)^{-1} H_{\boldsymbol{x}_{k,i}}^\top \bar{R}^{-1} \left(y_k - h\left(\boldsymbol{x}_{k,i}\right) - H_{\boldsymbol{x}_{k,i}} \left(\hat{\boldsymbol{x}}_{k|k-1} - \boldsymbol{x}_{k,i}\right)\right), \tag{4-20}$$

based on the equality of

$$\left(H_{\boldsymbol{x}_{k,i}}^\top \bar{R}^{-1} H_{\boldsymbol{x}_{k,i}} + P_{k|k-1}^{-1}\right)^{-1} H_{\boldsymbol{x}_{k,i}}^\top \bar{R}^{-1} = K_{\boldsymbol{x}_{k,i}} = P_{k|k-1} H_{\boldsymbol{x}_{k,i}}^\top \left(H_{\boldsymbol{x}_{k,i}} P_{k|k-1} H_{\boldsymbol{x}_{k,i}}^\top + \bar{R}\right)^{-1}. \tag{4-21}$$

Substituting this Kalman gain into Eq. (4-20) and we will have

$$\boldsymbol{x}_{k,i+1} = \hat{\boldsymbol{x}}_{k|k-1} + K_{\boldsymbol{x}_{k,i}} \left(y_k - h\left(\boldsymbol{x}_{k,i}\right) - H_{\boldsymbol{x}_{k,i}} \left(\hat{\boldsymbol{x}}_{k|k-1} - \boldsymbol{x}_{k,i}\right)\right). \tag{4-22}$$

For $i = 1$, we will set $\boldsymbol{x}_{k,1} = \hat{\boldsymbol{x}}_{k|k-1}$ which is exactly the EKF. By viewing the EKF as an optimization problem, we have gained the ability to iteratively enhance the estimation results and utilize optimization tools to analyze the performance of the estimation. The stopping criteria are set either the iteration reaches the maximum number of iterations or the difference between consecutive two iterations becomes trivial. After satisfying the stopping criteria, we will set $\hat{\boldsymbol{x}}_{k|k} = \boldsymbol{x}_{k,i}$.

The covariance matrix $P_{k|k}$ has been found to be the inverse of the Hessian matrix [51]

$$\mathbb{E}\left[\left(\hat{\boldsymbol{x}}_{k|k} - \boldsymbol{x}_k\right)\left(\hat{\boldsymbol{x}}_{k|k} - \boldsymbol{x}_k\right)^{\top}\right] = \left(G_{\hat{\boldsymbol{x}}_{k|k}}^{\top} \bar{Q}^{-1} G_{\hat{\boldsymbol{x}}_{k|k}}\right)^{-1}. \tag{4-23}$$

As $\hat{\boldsymbol{x}}_{k|k}$ is obtained after meeting the stopping criteria, we will compute Eq. (4-23) only after the last iteration in each time instance. Expanding Eq. (4-23), we will have the following equation for correction covariance update

$$P_{k|k} = P_{k|k-1} - K_{\hat{\boldsymbol{x}}_{k|k}} H_{\hat{\boldsymbol{x}}_{k|k}} P_{k|k-1}. \tag{4-24}$$

Chapter 5

Experiments

To validate the performance of the method using the kinetics model with IMUs on the human motion dataset, we have utilized a dataset from Swiss Paraplegic Research. IMUs and markers have been placed on the upper extremity with the right arm of the participants conducting wheelchair propulsion tasks. The sensors' setup and alignment will be specified in this chapter. The dataset we used includes four different tasks: desk work, treadmill propulsion, manual material handling, and dribbling. Detailed descriptions of these tasks are provided. Furthermore, we compared the estimation results obtained from different methods with the marker-based method as the benchmark. We will clarify the definition usage of these methods in this section.

5-1   Sensor Setup

All the sensors used in the experiments require a counterpart to be defined in the OpenSim which is referred to as "virtual sensors" in the previous study [19]. These "virtual sensors" are needed to be aligned well with our OpenSim model to track the signals measured during the experiments by the model.

5-1-1   Marker

In the dataset, virtual markers and experimental markers have been placed at different locations of the human body. To introduce the "virtual markers" used in our study, the concept of Bony Landmark (BLM) is needed. BLMs are anatomical structures or points on bones used as reference points for medical and anatomical measurements. In this dataset, BLMs were identified following the work of Wu et al. [38]. As the "virtual markers" are placed on the BLMs in the OpenSim model, we will refer to our "virtual markers" as BLM markers. On the other hand, the experimental markers used in our study are the actual measurements obtained through the use of an Optical motion capture system during the experiments. They
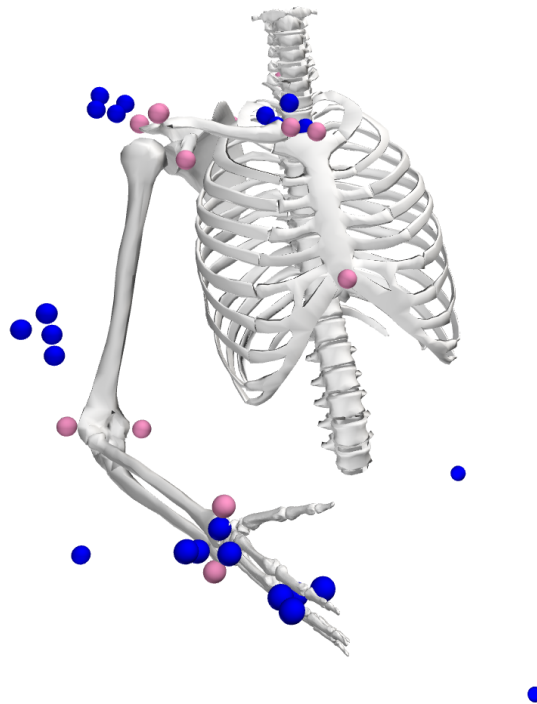
Figure 5-1: The BLM markers are shown in pink dots affixed to the body in the OpenSim model. The experimental marker cluster attached on the IMU is shown in blue dots. Only the BLM marker has been aligned with the OpenSim model. The blue dots that are not close to the human body model is attached to the wheelchair.

are used in the form of marker clusters, four markers are contained in each cluster. Clusters are attached on the IMUs which in turn has been placed on the human body.

In Fig. 5-1 we have shown the two different markers in pink dots and blue dots for BLM marker and experimental marker respectively. We can see the BLM markers affixed on the BLMs, while the experimental are not well aligned with the OpenSim model as no special process has been taken to obtain its alignment to the model.

The BLMs markers were utilized for IK and ID analyses and have already been aligned in the OpenSim model. As the human body is assumed to be rigid, the relative position of the experimental markers and BLM markers are fixed, therefore the data collector can derive the trajectory of BLM markers using experimental markers measurements. Another use of the experimental markers was for IMU alignment which will be specified in the following section.

5-1-2   IMU

As the IMU alignment with the OpenSim model is not pre-defined in the dataset, in this section we will focus on the process for IMU alignment which is a "Wahba's problem" [46]. A static trial is contained in the dataset with the participant conducting the pose depicted in Fig. 5-2, where only the forearm has a 90° flexion.

In our study, the alignment of the IMU is determined by first establishing the transformation from the IMU frame to the ground frame and then establishing the transformation from the
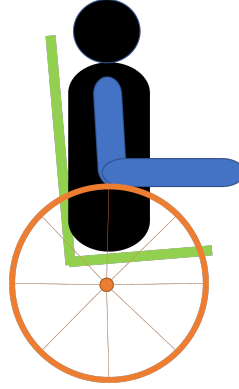
Figure 5-2: Figure showing the upper extremity of the subject maintained a stationary position on the sagittal plane.

ground frame to the segment frame. This process can be demonstrated as

$$^{i}R_{s_i} = {}^{i}R_0 \, {}^{0}R_{s_i}, \tag{5-1}$$

where $^{i}R_{s_i}$ is the IMU frame s_i alignment with the ith body of OpenSim, $^{i}R_0$ is the transformation from the ground frame to body frame, and $^{0}R_{s_i}$ is the transformation from IMU frame s_i to ground frame.

To determine the transformation from the IMU frame to the ground frame, we leveraged the marker cluster attached to the surface of the IMU frame. We needed to know the position of each marker in both the IMU frame and the ground frame. In the static trial, we measured and recorded the position of each marker in the cluster with respect to the ground frame as $^{0}p_{j,k}$, where $j = 1, 2, 3, 4$ represents each marker and k represents the time instance of the measurements. To obtain the position of the marker cluster in the IMU frame, we need to find the origin of the IMU frame. Additional markers located on the sides of the IMUs are used, as shown in Fig. 5-3a. We conducted another trial where the IMU was placed on a flat surface to locate the origin of the IMU with the help of additional markers. The origin and axes of the IMU frame are defined as depicted in Fig. 5-3b which is specified in the user manual [55]. With knowledge of the origin's location in the IMU frame and the marker cluster's location with respect to the ground frame, we derived the position of the marker cluster with respect to the IMU frame, as shown in Fig. 5-3b. Each marker cluster consists of four markers, and we represent its position in the IMU frame as $^{s_i}p_{j,k}$.

Knowing the position of marker cluster in both IMU frame and ground frame, we can obtain the ground-to-IMU transformation, represented by the rotation matrix $^{0}R_{s_i}$ and the translation vector $^{0}t_{s_i}$, using the following optimization problem

$$\underset{^{0}R_{s_i}, ^{0}t_{s_i}}{\arg\min} \sum_{j=1}^{4} \sum_{k=1}^{60} \left\| ^{0}R_{s_i} \, {}^{s_i}p_{j,k} + {}^{0}t_{s_i} - {}^{0}p_{j,k} \right\|_2^2, \tag{5-2}$$

which is a quadratically constrained quadratic programming problem solved by the Gurobi solver.
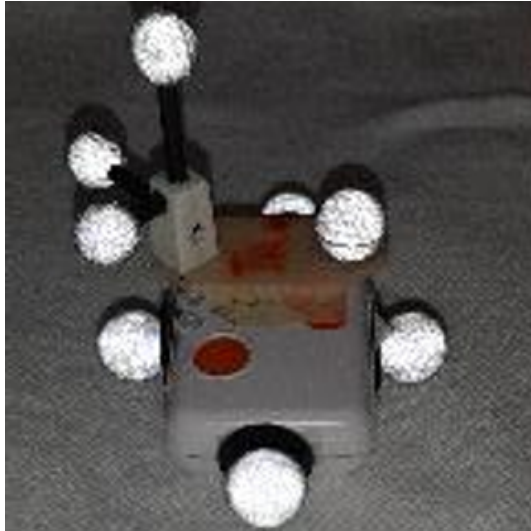
(a) Marker cluster placed on top of the IMU with four additional markers on the middle point of each side of IMUs. Additional markers are used to find the origin of the IMU frame expressed *w.r.t.* the ground frame.
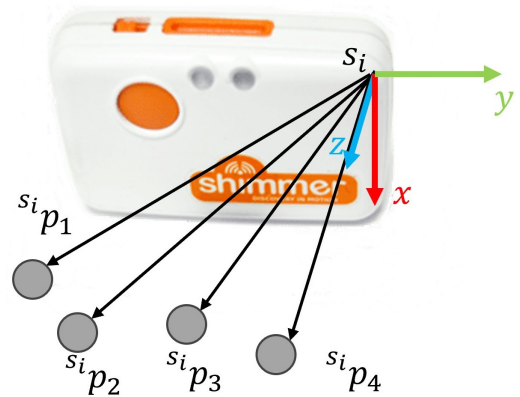
(b) The marker cluster position *w.r.t.* the IMUs body frame.

Figure 5-3: The relationship between the IMU and marker cluster are demonstrated.

The transformation from the ground frame to the body frame is determined based on IK using BLM markers in the static trial. The resulting transformation is denoted as ^0R_i and ^0t_i. Together with the acquired knowledge of $^0R_{s_i}$ and $^0t_{s_i}$, we can determine the IMU alignment to the OpenSim model. This procedure is performed for all three IMUs on the thorax, humerus, and forearm.

5-1-3   Force Sensor

In the previous work from J.Boelens [31], the force sensor also needs to be aligned with the OpenSim model. In our study, the force measurements are given in the dataset with their magnitude and position all expressed in the OpenSim ground frame. However, in our study, the model does not have the DoF for translation in 3-dimensional space, which is impossible to use the force measurements if the force position is moving in the ground frame. Considering all the tasks we selected, the participants only had external force at hand, we have fixed the force applied position to be always at the origin of our hand frame. The magnitude expressed in the OpenSim ground frame can be directly used for computing multibody dynamics.

5-2   Tasks Description

Four different tasks were used in this study, namely desk work, wheelchair propulsion on a treadmill, manual material handling, and dribbling. The abbreviations and descriptions of these tasks were provided by the work of W. Vries et al.[56] and are presented in Table 5-1.

Table 5-1: Description of motion used in our study.

Motion	Abbreviation	Description	Duration
Desk Work	Desk	While seated at a desk, engaging in activities such as typing on a keyboard, utilizing a mouse, and using a mobile phone.	42.13s
Wheelchair propulsion on a Treadmill	Treadmill	Continuous wheelchair propulsion on the treadmill at 0.56 and 1.11 m/s at 0%, and 0.56 m/s at 6% inclination.	171.94s
Manual Material Handling	MMH	The task involves picking up a 2 kg weight and placing it onto three separate shelves within a cupboard. The motion begins from a state of rest, as the hand initiates movement to grasp the weight for the first time, and continues until the weight is released upon completing the entire sequence.	61.58s
Dribbling	Dribbling	The activity involved intermittent wheelchair propulsion within a restricted space, where the distance covered was limited to a maximum of 3 meters. The propulsion consisted of a maximum of 3 pushes, including turns and backward propulsion. The activity commenced with the first rotation of the wheel and concluded when the wheel ceased to rotate.	33.39s

In the Desk Work task, there is no external force involved. In activities involving wheelchair propulsion, such as the treadmill or the dribbling task, external forces are exerted on the wheel, which includes a force sensor that measures three-dimensional force components. The external force in Manual Material Handling (MMH) is provided by the known material weight as the known input value o a step change signal. In desk work and MMH, the participants were asked to wave their arms quickly to synchronize the IMUs and marker position measurements at the beginning, referred to as the 'happy handshake' motion.

5-3   Comparison to Different Methods

To show the different characteristics of the kinematics mode and kinetics model, methods based on the kinematics model and OpenSense is used for comparison. The definition of these two methods and the hyperparameter setting of all the methods will be introduced in

this section.

5-3-1   Kinematics EKF

The kinematics model utilizes the same measurement model as our method, while the states are chosen to be generalized coordinates, velocities, and acceleration. The dynamic model becomes a constant acceleration model and is defined as

$$
\begin{bmatrix} \boldsymbol{q} \\ \dot{\boldsymbol{q}} \\ \ddot{\boldsymbol{q}} \end{bmatrix}_{t+1} = \begin{bmatrix} I_{N_q} & T & T^2/2 \\ 0 & I_{N_q} & T \\ 0 & 0 & I_{N_q} \end{bmatrix} \begin{bmatrix} \dot{\boldsymbol{q}} \\ \dot{\boldsymbol{q}} \\ \ddot{\boldsymbol{q}} \end{bmatrix}_t + \begin{bmatrix} T^3/6 \\ T^2/2 \\ T \end{bmatrix} \nu_k, \tag{5-3}
$$

where

$$
\nu_k \sim \mathcal{N}\left(0, Q_{\ddot{\boldsymbol{q}}}\right)
$$

and $Q_{\ddot{\boldsymbol{q}}}$ works as an indicator of how constant we expected the generalized acceleration to be during the motion. The smaller the $Q_{\ddot{\boldsymbol{q}}}$ the more constant $\ddot{\boldsymbol{q}}$ becomes. The EKF is used as the estimation algorithm. Since the kinematics can not estimate joint torque, a separate ID using `InverseDynamicsSolver` of OpenSim is needed to compute the joint torque.

5-3-2   OpenSense

To use OpenSense, multiple algorithms are cascaded to generate the estimation. Before running OpenSense, it is necessary to determine the orientation of the IMUs with respect to the ground frame. To estimate the IMUs orientation, we employed the Madgwick filter [23], which relies on magnetometer measurements. OpenSense utilizes the orientation of the IMUs as inputs to a nonlinear least square problem of

$$
\arg\min_{\boldsymbol{q}_1,\cdots,\boldsymbol{q}_{N_q}} \sum_i^n \left\| w_i \alpha_i \left(\boldsymbol{q}_1, \cdots, \boldsymbol{q}_{N_q} \right) \right\|_2^2, \tag{5-4}
$$

where $\boldsymbol{q}$ is the generalized coordinates, α_i represents the orientation of the ith IMU, and w_i is the weight term assigned to the ith IMU. The OpenSense is solved using OpenSim function `IMUInverseKinematicsTool`. As OpenSense focuses solely on estimating generalized coordinates, additional steps of ID are also required. We differentiate the generalized coordinates twice to obtain the generalized velocities and accelerations. To mitigate the effects of noise in the signals, a 6 Hz low-pass filter is implemented.

5-3-3   Marker IK/ID

Marker IK/ID was performed using OpenSim GUI tools, specifically the Inverse Kinematics and Inverse Dynamics tools. Since the trajectory of BLM markers is expressed in the 3-dimensional ground frame, the model we used for Marker IK/ID has translational DoF in the ground frame. To refine the results obtained from the Inverse Kinematics tool, a 6 Hz low-pass filter was applied.

5-3-4   Overview of all the Methods used in the Experiments

Table 5-2: Characteristics of the method used in this thesis. ϵ denotes the stopping criteria used for the iterative estimation algorithm. **w** represents the weight assigned to different sensors for Marker IK/ID and OpenSense.

Methods	System Model	Tuning Parameters
Kinetics EKF	Kinetic	$Q_q, Q_{\dot{q}}, Q_\tau, Q_f, R_{s,a}, R_{s,\omega}$
Kinematics IEKF	Kinetic	$Q_q, Q_{\dot{q}}, Q_\tau, Q_f, R_{s,a}, R_{s,\omega}, \epsilon$
OpenSense	Kinematic	**w**
Kinematics EKF	Kinematic	$Q_{\ddot{q}}, R_{s,a}, R_{s,\omega}$
Marker IK/ID	Kinematic	**w**

The characteristics of the methods employed in this thesis are summarized in Table 5-2. The Kinetics EKF and Kinematics IEKF methods represent the method we adapted from previous work of De Kanter [19] leveraging the kinetics model of the human body. Kinematics EKF describes the methods introduced in section 5-3-1.

In the case of OpenSense, the tuning parameter **w** allows for assigning different weights to individual IMUs. For our study, we have set **w** to a uniform value of 1 for all IMUs. The stopping criteria for Kinematics IEKF is set to maximum of 10 times of iteration or the difference between two iterations is smaller than 1×10^{-5}.

5-4   Hyperparameter Setting of the Filters

For EKF and IEKF based methods, only the relative setting of the hyperparameter matters. There are several relative values have been tested during the tuning process: the weighting between the noise covariances of specific force R_{s,a_i} and angular velocity measurements R_{s,ω_i}, the noise covariance between IMU on different segments, and the weighting between the noise covariance of measurements and the process noise covariance. It is worth noting that the optimal tuning parameters can vary across different motion scenarios. As a result, the numerous relative weightings make tuning the hyperparameter settings a challenging task.

Table 5-3: Table of hyperparameter setting for the measurements noise covariance.

Measurement Noise					
R_{s,a_1}	R_{s,ω_1}	R_{s,a_2}	R_{s,ω_2}	R_{s,a_3}	R_{s,ω_3}
2.59×10^1	4.04×10^{-3}	2.59×10^1	4.04×10^{-1}	2.59×10^1	4.04×10^{-1}

To find the optimal setting, we have adjusted the relative weights between R_{s,a_i} and R_{s,ω_i} and IMU on different segments as in Table 5-3. This measurement covariance setting is fixed through four different tasks. The value for IMU measurements covariance is scaled based on the IMU user manual [55]. The R_{s,ω_i} has been set smaller than R_{s,a_i} as we expect the specific force including acceleration measurements to have more fluctuation measurements. The R_{s,ω_1} has been set smaller than R_{s,ω_2} and R_{s,ω_3} as we expect the motion of the thorax body will

be less dynamic and fluctuated. Note that on the same IMU every axis has the same noise covariance value. Also, Kinetics EKF and Kinematics EKF used the same covariance values of measurement noise. Based on the setting in Table 5-3, we have tested different covariance value setting scenarios for process noise covariance Q, which will be demonstrated in the next chapter.

Chapter 6

Results

This chapter presents the results of our proposed method, which combines the model defined in Chapter 3 with the estimation method of EKF introduced in Chapter 4. Firstly, we assess the effectiveness of our proposed framework by comparing it to the baseline method for three distinct tasks. We analyze the observed phenomena and further investigate at specific time instances by adjusting hyperparameters to gain insights into the behavior of our proposed method. Secondly, we conduct a comparative analysis by evaluating our proposed method against kinematics-based approaches and OpenSense to determine its performance. Note that the results of the Desk task can be found in Appendix A-3.

6-1 Experimental Validation with Abrupt External Load Variations

During the MMH task, as the participant engages in grabbing and placing a weight on the shelves, the rapid changes in the input signal representing external forces can pose a challenge for our system, as the states need to react quickly. Although the input signal is artificially set by measuring the weight being held in hand prior to the experiments, this scenario serves as a meaningful test to demonstrate the method's characteristics. Consequently, we have introduced various hyperparameter adjustments, as presented in Table 6-1.

Table 6-1: Table of hyperparameter setting for the MMH task.

Scenarios	Process Noise		
	Q_q	Q_f	Q_τ
s1	1×10^{-6}	1×10^3	1×10^4
s2	1×10^{-6}	1×10^3	1×10^8
s3	1×10^{-6}	1×10^{-6}	1×10^8

The definitions of Q_q, Q_f, and Q_τ are provided in Eq.3-8. All scenarios utilized the same measurement noise covariance value with the same Q_q. When comparing these three scenarios,

both s1 and s2 shared the same Q_f, while s1 had a smaller Q_τ. For s2 and s3, they shared the same Q_τ, but s2 had a larger Q_f. The corresponding RMSD values compared to the Marker IK/ID are presented in Table6-2. Regarding joint angle estimation, s1 exhibited the lowest overall RMSD when compared to Marker IK. For joint torque estimation, s3 yielded the lowest RMSD. However, since the Marker IK/ID method serves as a baseline rather than the ground truth, we generated Fig. 6-1 to explore the temporal behavior of the estimation across the three scenarios.

Table 6-2: The RMSD for 3 different hyperparameter tunning scenarios.

(a) Joint Angle

Scenarios	Joint angle RMSD [°]								Overall
	q_1	q_2	q_3	q_4	q_5	q_6	q_7	q_8	
s1	4.75	4.95	5.74	12.35	5.89	22.23	19.80	26.35	12.75
s2	4.33	5.05	4.71	20.36	12.47	39.31	20.72	25.94	16.61
s3	4.38	5.32	9.08	16.53	9.54	29.64	19.13	27.62	15.16

(b) Joint Torque

Scenarios	Joint torque RMSD [Nm]								Overall
	τ_1	τ_2	τ_3	τ_4	τ_5	τ_6	τ_7	τ_8	
s1	5.22	5.72	3.33	2.18	1.71	1.81	1.39	0.32	2.71
s2	4.33	6.66	2.66	3.05	2.38	1.72	1.35	0.31	2.81
s3	4.61	5.99	2.66	2.13	1.87	1.51	1.30	0.31	2.55

In Fig.6-1, the plotted joint torque estimations encompass τ_3 (thorax rotation) and τ_4 (shoulder flexion). We chose to include τ_3 in the plot to show how the estimation from the Marker IK/ID method exemplifies noise after differentiation. Additionally, we selected τ_4 as it represents shoulder flexion, a joint highly pertinent to the MMH task of grabbing and placing weights on the shelves in front of the participant. Within Fig.6-1, the blue shaded area designates the period during which the participant held the weight in their hand. Furthermore, annotated text arrows pinpoint the seven instances where the weight was held during the experiments.

When examining the joint torque estimation while the participant is holding the weight, as illustrated in the first and second columns of the zoomed-in plots in Fig.6-1, it becomes evident that torque estimation oscillations occur during the actions of grabbing or placing the weight in scenario s3. Notably, the s3 scenario exhibits an underdamped response to the step change in the input signal. By maintaining a larger Q_τ and increasing Q_f, the s2 scenario mitigated the underdamped behavior while retaining a rapid response. This suggests that applying a higher input noise covariance results in increased damping in the transient of joint torque estimation, possibly by allowing joint velocity to adapt to the input signal change. As seen from Eq.(4-14b), a larger Q_f implies greater covariance of the input signal and reduced confidence in the prediction of joint velocity. In the s1 scenario, a smaller Q_τ yields an overdamped response, showcasing a smoother estimation curve while achieving a lower RMSD compared to s2.

While s2 enables responsive estimation without oscillation, it does not yield the smallest RMSD for joint angle estimation due to an offset in estimation. This can be explained by
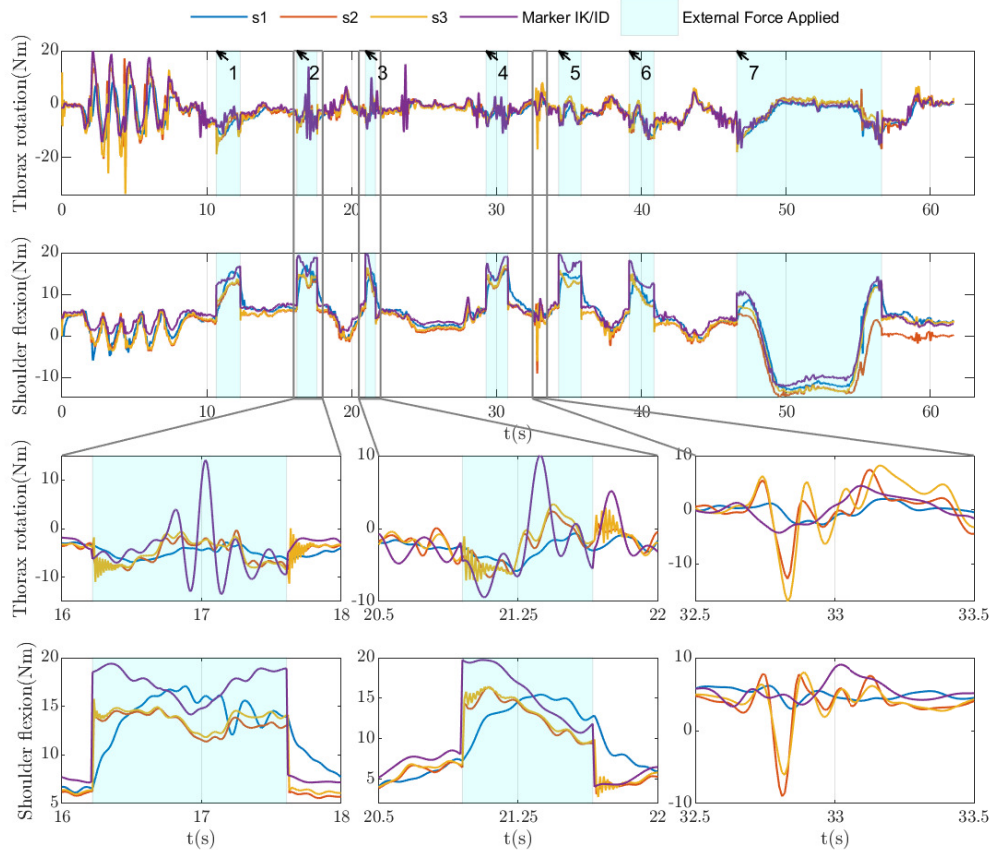
Figure 6-1: Zoomed-in plots depicting the behavior of thorax rotation and shoulder adduction joint torque estimation during the MMH task. Three scenarios of hyperparameter setting are employed to investigate the behavior of our method reacting to a step change in the external force signal.

the fact that within each blue-shaded area represents the duration of weight holding the s2 scenario displays a static state error. When compared to s2 and s3, the s1 response to the step change is slower but exhibits a smaller offset when the weight is held in hand.

In the first and second columns of the zoomed-in plot, oscillations were observed in the estimated thorax rotation torque obtained through Marker IK/ID when no external force interaction was present. To clarify this phenomenon, we present Fig. 6-2, where oscillation occurrences are indicated by vertical dotted lines at t = 16.95s and 21.25s. Analysis revealed that during these instances, the joint angle estimation exhibited slight jumps, possibly due to noise or marker position measurement occlusions. Consequently, significant peaks in angular velocity were computed through angle differentiation, even though a 6 Hz low-pass filter was applied. The utilization of these noisy angular velocity values for torque computation in ID contributed to the observed oscillatory behavior.

The third column of the zoomed-in plot demonstrates the property of Kinetics EKF. As depicted in the third column of the zoomed-in plot, fluctuations in joint torque were also observed in the estimated values obtained from our proposed method. Through careful ex-
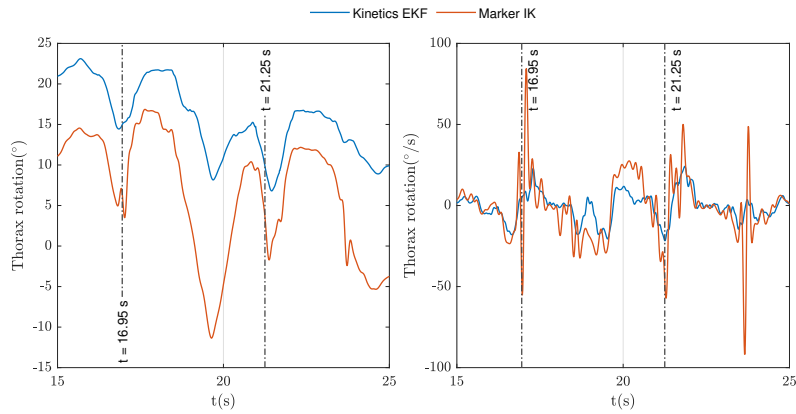
Figure 6-2: Plot of the Marker IK/ID estimated thorax rotation angle (right) and velocity (left). The vertical gray lines indicate the time instance corresponds to the peak value observed in joint torque estimation. The peak in joint velocity estimation results from the numerical differentiation of the joint angle, which suggests the downside of the Marker IK/ID method.

amination of the experiment's video recording, we discovered that the slight arm-swinging motion generated by the participant was captured by our method in scenarios s2 and s3, while no discernible results show on Marker IK/ID and s1 scenario of our method. Fig. 6-3 further supports the observed arm-swinging motion, as the IMU on the forearm measured a change in specific force and angular velocity between t = 32.5s and t = 33s. It is important to note that IMUs measurements at the forearm will influence the humerus and thorax joints estimation. This finding highlights the ability of our algorithm to capture the slight motion when a higher value of Q_τ is employed. Conversely, the Marker IK/ID was unable to detect this subtle motion due to the use of a low-pass filter, which filtered out useful information.
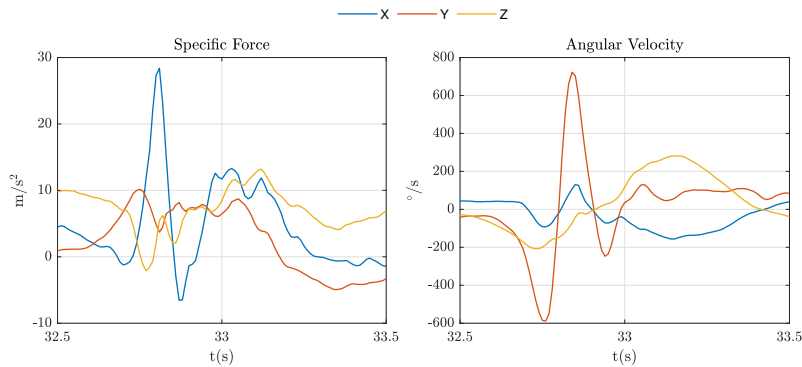
Figure 6-3: Plot indicating the time instance of the arm-swinging of the participants has been captured by IMU measurements on the forearm. This slight movement has also been captured by the Kinetics EKF method when a higher Q_τ is employed.

Simulated IMUs Signal Evaluation for MMH Task

In this section, we will compare the simulated IMUs signal as shown in Eq. (3-12) to the measured IMU signal to see if the algorithm is tracking the measurements. Fig. 6-4 provides

visualization of the x-axis IMU measurement signals for the forearm, humerus, and thorax during MMH task. Each scenario in the specific force prediction reveals the presence of a peak in the simulated IMU signals when an external force is applied. Again, s3 exhibits the severest oscillation, and the oscillation is mitigated in the s2 scenario. s2 and s3 both have a fast yet fluctuating response, while s1 is overdamped and it takes longer time to converge in s1.
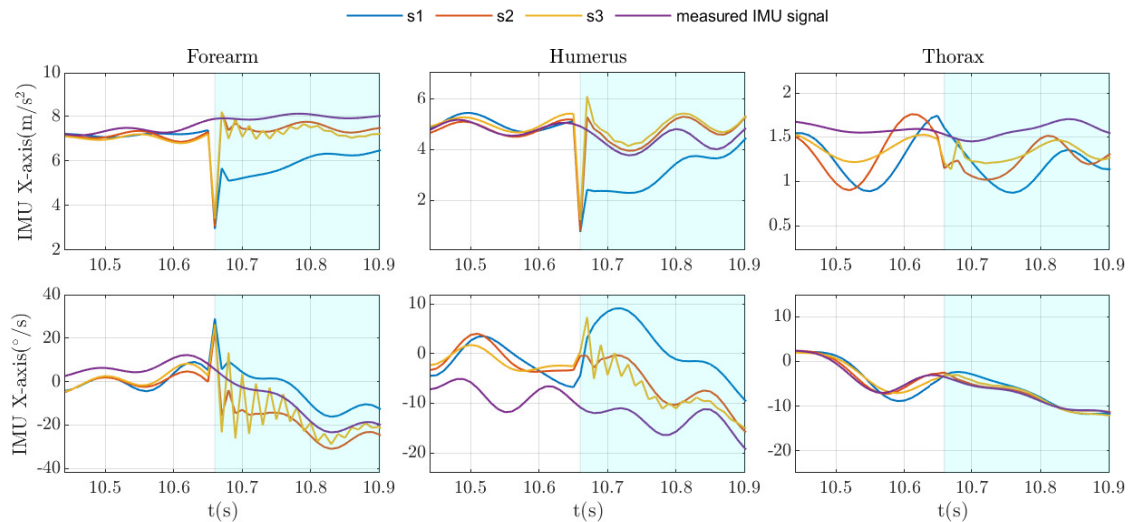
Figure 6-4: Predicated x-axis IMUs signal attached on forearm, humerus, and thorax during MMH task. Specific force and angular velocity signals are represented in the first and second rows respectively.

Remarkably, this oscillatory behavior is most prominent in the forearm IMU, while it appears relatively weaker in the thorax IMU and is even absent in the angular velocity prediction for the thorax. This observation can be explained by the external force being exerted on the hand, which can be regarded as the same rigid body as the forearm due to the wrist being a weld joint.

6-2 Experimental Validation Using Kinetics IEKF

As we introduced in chapter 4, the iterative version of EKF, i.e. IEKF is used to see whether iteration within each instance will increase the estimation accuracy. The stopping criteria are set as a maximum of 10 times of iteration or the difference between two iterations is smaller than 1×10^{-5}.

In Fig. 6-5 we demonstrate the results of using IEKF as the estimation algorithm compared to EKF, using Marker IK/ID as the benchmark. The same three hyperparameter setting scenarios were used on the shoulder flexion torque estimation.

In the overdamped scenario, s1, the improvement in torque estimation is not evident in Kinetics IEKF. The error is even increased during the instance without holding the weight. In the s2 scenario, the response to the external force signal is still fast and the static error is diminished for both holding or not holding the 2kg weight. In underdamped scenarios, s3,

the static error for the duration of not holding the weight is decreased with the zoomed-in plot showing that the oscillation is escalated in response to the external force signal.

This demonstrates that the IEKF is not guaranteed to improve the estimation of joint torque, it also depends on the setting of the hyperparameter. For overdamped and underdamped setting scenarios, the improvement in estimation accuracy is limited, as shown in Table 6-3. The only scenario that has benefited from the use of IEKF is highlighted by the lavender row color. The improvement in estimation accuracy is most prominent using IEKF only when the hyperparameter setting does not show intense oscillation while reacting promptly.

Table 6-3: Comparison between Kinetics EKF and IEKF on 3 different scenarios for joint angle and torque estimation. Only in s2 scenarios the estimation is improved by IEKF.

	Joint Angle(°)		Joint Torque(Nm)	
Scenarios	EKF	IEKF	EKF	IEKF
s1	12.75	13.43	2.71	2.96
s2	16.61	13.08	2.81	2.45
s3	15.16	16.14	2.55	2.77
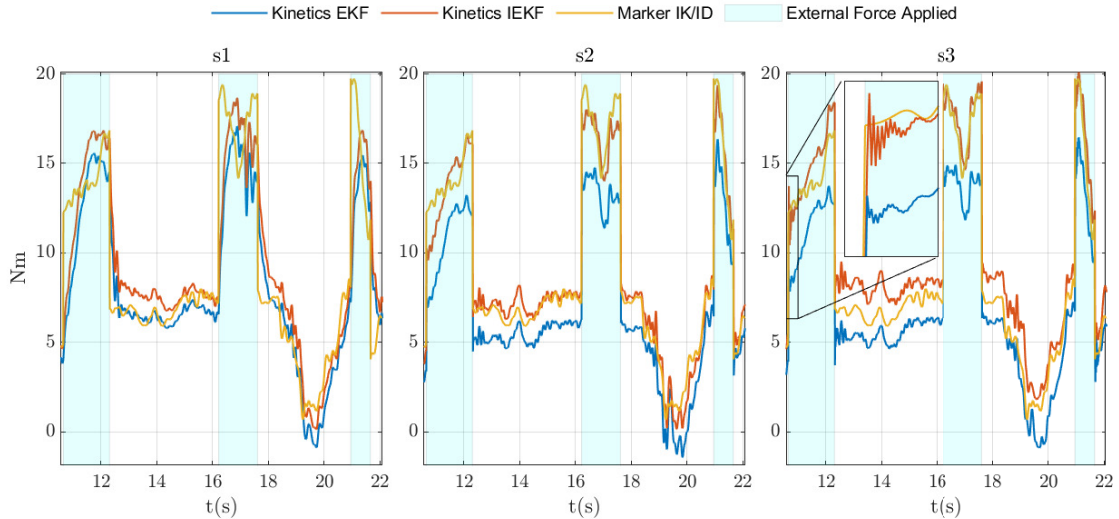
Figure 6-5: Kinetics EKF and Kinetics IEKF were employed to estimate shoulder flexion torque during the first three instances of grabbing and placing a 2 kg weight, in comparison to Marker IK/ID. In the overdamped scenario s1, the IEKF results in a constant error during the instance when the participant was not holding the weight. In the s2 scenarios, the static error present in the EKF algorithm is reduced when holding the weight in the IEKF. As for the s3 scenario, where $Q_\tau = 1 \times 10^8$, although the static error is also diminished, the zoomed-in plot illustrates that the oscillation in estimation is amplified in the IEKF compared to the EKF.

6-3   Experimental Validation on Highly Dynamic Task

The Treadmill task represents the most dynamic task that has been tested during the experiments. The hyperparameter setting found by the author generates the lowest RMSD in

estimation accuracy compared to Marker IK/ID is shown in Table 6-4.

Table 6-4: Table of hyperparameter setting for the Treadmill task.

| | Process Noise | | |
Method	Q_q	Q_f	Q_τ
Kinetics EKF	1×10^{-6}	1×10^5	1×10^5

The resulting RMSD of kinematics, kinetics, simulated IMU signal estimation is given in Table A-5. However, for joint angle estimation, this overall RMSD does not fully capture the profile of our estimation results. As depicted in Fig. 6-6, the Mean Absolute Difference (MD) with the red line of its linear fit for joint angle estimation in these five joints suffers from severe fluctuation. The MD fluctuates in the range of $40°$, $80°$, $100°$, $40°$, and $60°$ for the joints of thorax rotation, shoulder flexion, shoulder rotation, forearm flexion, and forearm rotation respectively. Notably, the drifting behavior began around 60 seconds for the first three shown joints here, with another turning point occurring around 100 seconds. This time instance coincides with the time of increasing the speed and inclination angle of the treadmill. Among the drifting joints, shoulder rotation showed the largest MD.

Table 6-5: RMSD for joint angle, velocity, and torque estimation for the Treadmill task. The reprojection error characterized by specific force and angular velocity prediction is also shown.

Method	Joint Angle RMSD(°)	Joint Velocity RMSD(°/s)	Joint Torque RMSD(Nm)	Specific Force RMSD(m/s²)	Angular Velocity RMSD(°/s)
Kinetics EKF	20.79	52.64	5.48	6.80	33.34
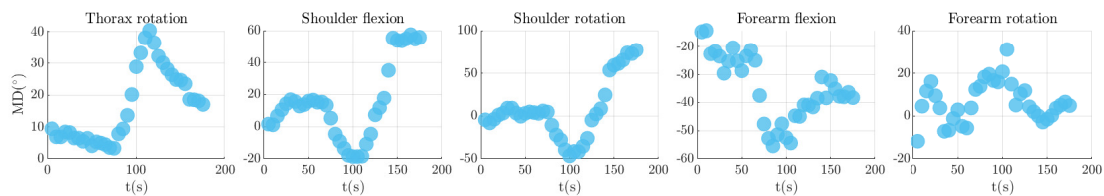
Figure 6-6: MD of the Treadmill task for 5 different joints. Each blue dot represents the MD of the joint angle estimation every 5 seconds.

The poor behavior in joint angle estimation can be explained by the large RMSD in joint velocity estimation, as we integrate joint velocity to get joint angle estimation. The author suspects that the Soft Tissue Artefacts (STA) is the cause, which will be explained in the next section. For more estimation performance reader on the Treadmill task, the reader is referred to Appendix A-5.

6-3-1   Validation of IMU Measurements Using Marker IK

To investigate the cause of degradation in joint angle and velocity estimation during the Treadmill task, Fig. 6-7 is presented. Fig. 6-7a shows the joint velocity estimation of Kinetics EKF against the numerical differentiation of Marker IK. In Fig. 6-7b, we have plotted the

simulated IMU measurements using Marker IK against experimental IMU measurements for the Y-axis of angular velocity on the humerus. We have zoomed into the time instance when the joint angle first exhibit increase in MD compared to Marker IK, between 65-72 seconds.
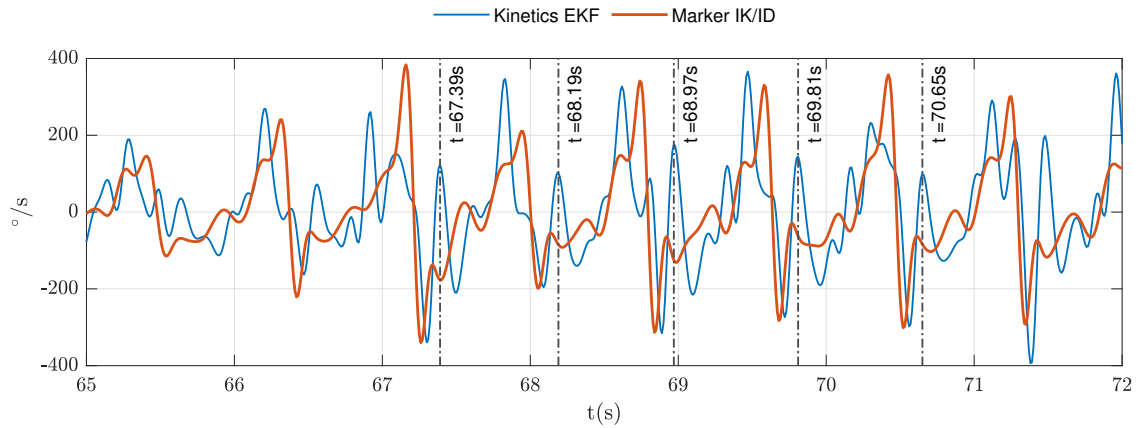
(a) The joint velocity estimation from Kinetics EKF is plotted against numerical differentiation of Marker IK. The instances where unexpected peaks are exhibited are denoted using vertical dotted lines showing specific time instances.

(b) The simulated IMUs angular velocity measurement from Marker IK is plotted against the experimental IMU measurements. The same time instance in Fig. 6-7a is also denoted in the plot to show the correspondence of erroneous IMU measurements and joint velocity estimation of Kinetics EKF.

Figure 6-7: The large RMSD in joint velocity estimation and unexpected peaks is shown in Fig. 6-7a. We investigated into the possible erroneous IMUs measurements demonstrated in Fig.6-7b.
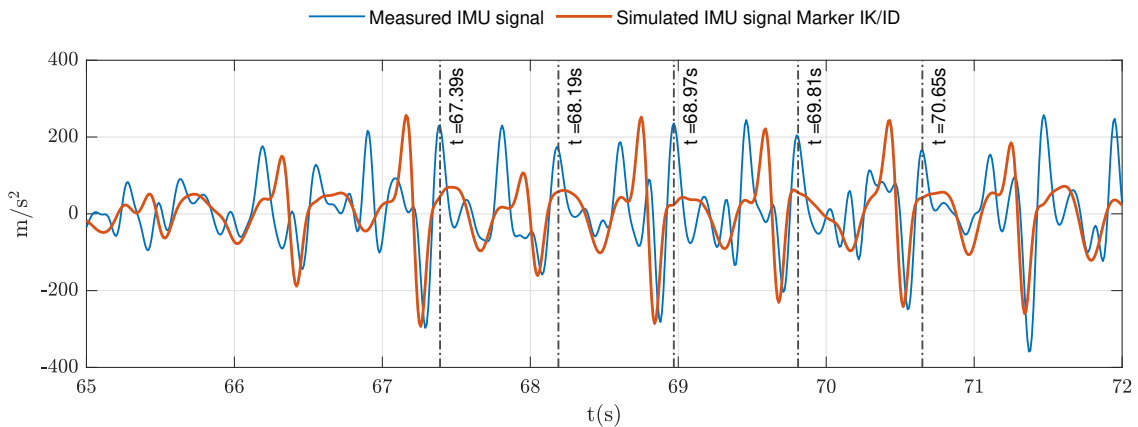
In Fig. 6-7a, we can observe a periodic pattern for joint velocity estimation of both methods. However, compared to Marker IK, Kinetics EKF estimation constantly results in unexplainable peaks in each wheelchair propulsion cycle especially starting from 67 seconds, as denoted by the vertical line. In Fig. 6-7b, the Marker IK simulated IMU measurements still show a clear periodic pattern, which is less clear in the experimental measurements from the IMU. At those time instances where unexplainable peaks exist, the experimental IMU also measures large angular velocity value for up to 200°/s, which has a large difference to Marker IK simulate IMU measurements.

The Treadmill task involves highly dynamic wheelchair propulsion movements. This dynamic

nature arises from the need to continuously generate forces to overcome resistance, accelerate, and decelerate. Additionally, wheelchair propulsion often involves repetitive and vigorous upper extremity movements, particularly in the shoulders, arms, and hands. These movements can result in the relative movement between the soft tissue and the skeleton, which is also known as STA. STA occurs when there is movement or deformation of the soft tissues, which can affect the accuracy and reliability of measurements from the wearable sensor. With this knowledge and the analysis we gave for Fig. 6-7, we determine that the STA has affected our estimation accuracy for joint angle and velocity in the Treadmill task.

6-4   Comparison Between Different Methods

In the previous section, we studied the performance of Kientics EKF compared to the baseline method Marker IK/ID. In this section, we will dive into the comparison between the methods utilizing IMUs for kinematics and kinetics estimation, namely Kinetics EKF, Kinematics EKF, and OpenSense. The task of dribbling is used for comparison, while Marker IK/ID serves as the benchmark, as we intend to utilize tasks with external factors for comparison. Kinematics EKF faces difficulties in finding a suitable tuning scenario for convergence with tasks like MMH and Treadmill.

6-4-1   Estimation Performance Evaluation: Kinetics EKF vs. Kinematics EKF vs. OpenSense

The noise covariance for process and measurements need to be tuned for Kinetics EKF and Kinematics EKF. The noise covariance of measurements is set to the same for both methods as given in Section 5-4, while the process noise covariance is varied to achieve the lowest RMSD in joint angle estimation compared to Marker IK. The resulting RMSD for joint angle and torque compared to Marker IK/ID is given in Table 6-6.

Table 6-6: Comparing RMSD of state estimation between different methods using Marker IK/ID as benchmark.

(a) Joint angle

				Joint angle RMSD [°]					
Methods	q_1	q_2	q_3	q_4	q_5	q_6	q_7	q_8	Overall
Kinetics EKF	3.13	7.07	18.22	7.53	3.95	6.06	14.52	28.52	11.13
Kinematics EKF	4.01	8.99	22.66	6.63	9.49	21.04	21.18	28.64	15.33
Opesense	3.35	6.30	4.88	11.53	12.33	24.80	7.30	11.34	10.23

(b) Joint torque

				Joint torque RMSD [Nm]					
Methods	τ_1	τ_2	τ_3	τ_4	τ_5	τ_6	τ_7	τ_8	Overall
Kinetics EKF	6.02	5.04	1.95	1.83	1.72	0.73	1.14	0.08	2.31
Kinematics EKF	14.41	6.01	2.26	1.89	2.46	1.26	2.04	0.11	3.81
Opesense	4.21	5.18	2.03	2.79	2.73	2.20	1.88	0.16	2.65

In Table 6-6, the RMSD is given for all joints with the index from 1 to 8 defined in Table 3-1. Analyzing the overall RMSD of joint angle estimation across these three methods, as shown in Table 6-6a, we observed that the Kinetics EKF has a very similar RMSD compared to OpenSense which utilizes heading information from a magnetometer. On the other hand, the Kinematics EKF exhibited the highest overall RMSD. This demonstrates the inclusion of Kinetics information has improved accuracy and robustness in kinematics estimation, which can yield similar accuracy compared to a method that leverages heading information. Note that although the same IMU alignment is used in these three methods, the Kinetics EKF has the most accurate shoulder rotation joint angle estimation while degrading in forearm joint angle estimation compared to OpenSense.

Turning our attention to joint torque estimation, presented in Table 6-6b, the Kinetics EKF shows a very close estimation compared to Marker IK/ID, yielding the lower RMSD compared to OpenSense. Kinematics EKF continued to exhibit the largest overall RMSD, particularly for τ_1, the thorax tilt joint torque estimation.
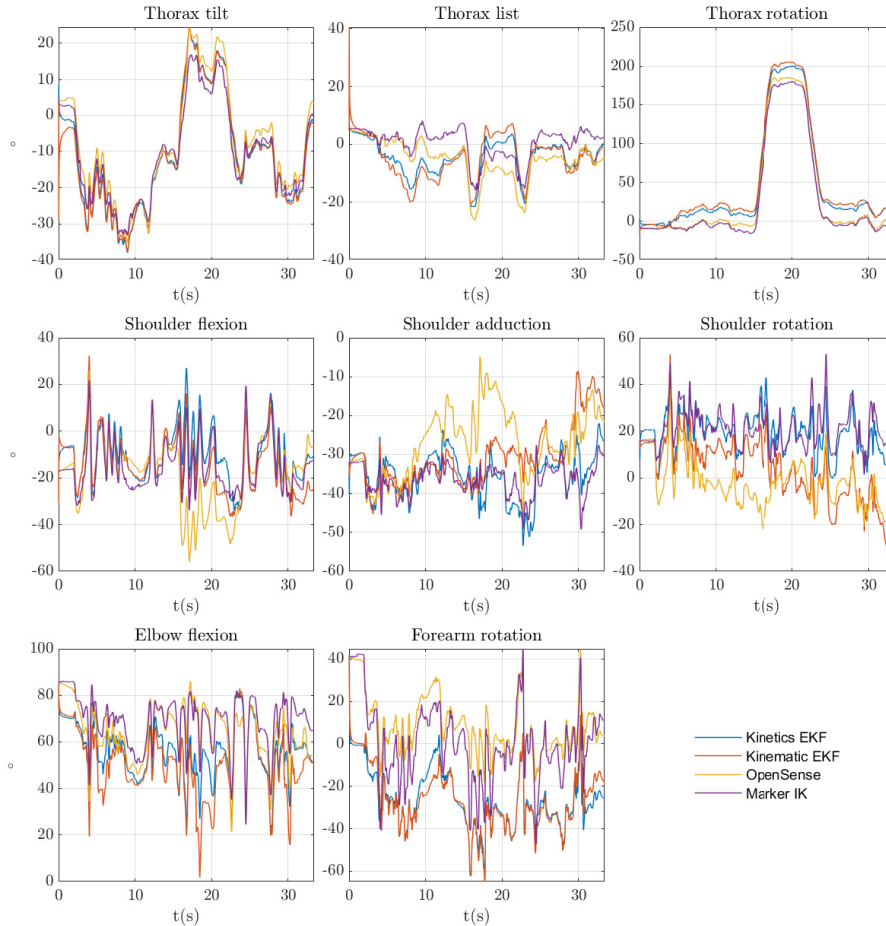

Figure 6-8: Comparison of joint angle estimation for Kinetics EKF, Kinematics EKF, and OpenSense during the Dribbling task.

To illustrate the temporal behavior of the three methods, we present Figures 6-8. Figure 6-8 displays the joint angle estimation for all joints throughout the entire duration of the Dribbling

task. Kinematics EKF exhibits larger overshoot at the initial time instances, especially for the thorax tilt and thorax list joints. It can also be observed that Kinematics EKF is more prone to drift, especially in all shoulder joint angles. This proves the benefits of including kinetics knowledge in the model. The OpenSense is able to yield the most accurate thorax rotation joint estimation by leveraging the use of a magnetometer. However, RMSD of the shoulder adduction and rotation joint angle estimation from OpenSense is the largest, probably due to the disturbance in the wheelchair or STA.

6-4-2   Model Difference Between Kinetics EKF and Kinemtics EKF

In the previous section, we analyzed the estimation performance comparing Kinetics EKF to other methods using IMU and the kinematics model. In this section, we will dive into the analysis of the essential model difference between the kinetics and kinematics model used for human task estimation regarding the differences in IMU simulated signal from the methods and the measurements Jacobian matrix.

Simulated Specific Force Signals

For both Kinematics EKF and Kinetics EKF methods, the simulated specific force signals are compared to the experimental specific force of IMU on the forearm in Fig. 6-9. It becomes evident that the simulated specific force signal from the Kinetics EKF method is affected by noisy input signals from external force measurements, as shown in Eq. (3-12). On the other hand, for the Kinematics model, the force is not a factor in the EKF, but in the subsequent ID process. The fact that the noise from force measurement is affecting the EKF algorithm for the Kinetics model could be solved by modeling external force as part of the measurements rather than the input of the system.

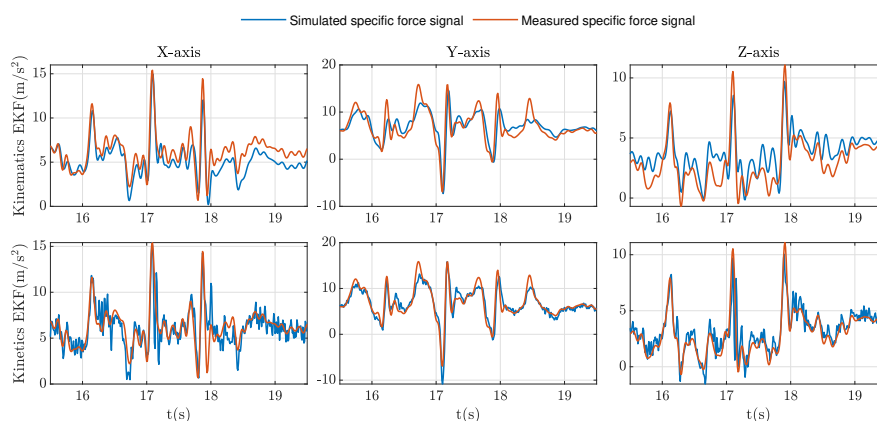

Figure 6-9: Simulated specific force signal on the forearm for Kinematics EKF and Kinetics EKF is plotted against the experimental specific force signal. The Kinetics EKF simulated specific force signal is affected by the noisy input signal.

Jacobian of the Measurements Model

Given the highly nonlinear nature of the measurement models for both Kinematics EKF and Kinetics EKF, the relationship between the states and the IMU measurements is not immediately obvious. Therefore, in this section, we will utilize the Jacobian of the measurement model to explore the distinctions in the mapping of measurements to states for both methods.

As depicted in Fig.6-10, two heat maps display the Jacobian matrices of the measurement models for both methods. Rows in Fig.6-10a and Fig. 6-10b correspond to IMU signals attached to the thorax, humerus, and forearm. Each column represents a state of the system—angle, velocity, and torque (or acceleration)—arranged from left to right, representing proximal to distal joints.

In the case of the Kinematics EKF, it is evident that specific force measurements on the thorax solely influence the states of thorax joints, while measurements on the forearm affect all the states of the system. On the contrary, the Kinetics EKF results in the specific force measurements from all segments influencing all the states. As a greater number of states can be affected by specific force measurements, this could be a plausible explanation for the enhanced robustness observed in the Kinetics EKF. However, for angular velocity measurements, as they cannot be directly derived from acceleration or torque states, the incorporation of a kinetics model does not lead to structural improvements.

In Fig.6-10a, the colored elements in the heat map indicate that in the Kinematics EKF, all IMU measurements are most sensitive to the joint angle states. Fig.6-10b reveals that in the Kinetics EKF, IMU measurements on the forearm exhibit higher sensitivity to joint angle compared to other IMU measurements on different segments. Notably, the IMU on the forearm displays significant sensitivity to the states of the forearm joint torque, which might account for the fluctuation of the simulated IMU signal on the forearm shown in Fig. 6-4.

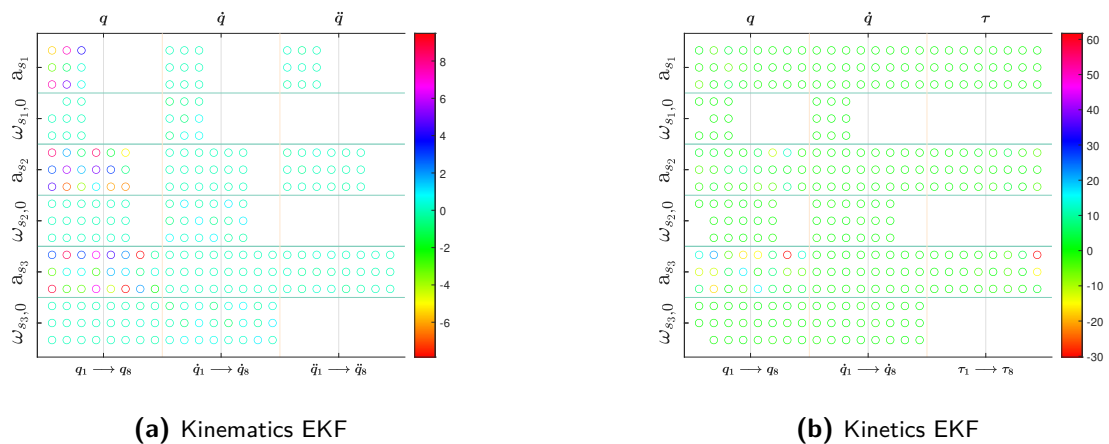(a) Kinematics EKF   (b) Kinetics EKF

Figure 6-10: The Jacobian matrix of the system measurement model for Kinematics EKF and Kinetics Extended Kalman Filter (EKF), where the element smaller than 1×10^{-9} has been set to zero.

6-5   Summary

In this chapter, we have showcased the performance of Kinetics EKF in several aspects during the tests on different tasks.

In the MMH task, where a step-like external force signal was artificially introduced, the tuning of Q_f and Q_τ played a crucial role in finding a balance between responsiveness and minimal vibration. By assigning less importance to the joint velocity prediction, we observed that the joint torque could react and converge quickly. This finding led us to have less confidence in the joint velocity prediction. This is possibly due to that when the external forces increased, our system model prediction is inclined to rely primarily on kinematics to counteract the external force. Assigning less confidence in the joint velocity prediction will let the correction step in the EKF change joint velocity and torque together to achieve higher accuracy. On the other hand, by using a large value for Q_τ, our algorithm demonstrated the ability to estimate subtle changes in joint torque resulting from nuanced motion. In contrast, the Marker IK/ID method failed to capture this information due to the implementation of a low-pass filter for joint velocity computation. The IEKF has also been tested on Manual Material Handling (MMH) motion, where significant improvement is observed by minimizing the static error while holding the weight. At the same time, the behavior of the Iterative Extended Kalman Filter (IEKF) is also highly dependent on hyperparameter tuning.

In the Treadmill task, the estimation accuracy was degraded. Interestingly, the setting that exhibited the poorest tracking performance of the IMU signal demonstrated the highest estimation accuracy. Furthermore, unexpected peak intermittently shows up in each propulsion cycle. This observation motivated us to investigate the source of these discrepancies, leading us to explore the reliability of the IMU measurements. Utilizing Marker IK simulated IMU signals, we discovered the presence of possible erroneous measurements in the IMUs measured signal up to 200° differences, which we believe to be a consequence of STA.

When comparing our proposed framework to other IMU and kinematics-based methods using the Dribbling task, we observed that Kinetics EKF exhibited close estimation accuracy compared to OpenSense, while excluding the use of a magnetometer. Compared to Kinematics EKF, Kinetics EKF consistently shows superior performance in terms of estimation accuracy. Furthermore, when we compared the model structure of the Kinetics EKF to the Kinematics EKF method, the incorporation of kinetics knowledge in our framework influenced the IMU prediction signal. Our proposed framework employed a denser measurement Jacobian matrix, potentially contributing to a more robust system while introducing some additional noise in the estimation process. This noise signal originates from the noisy external force measurements used as the system input signal.

Conclusion, Limitations, and Future Works

To address the research question posed in Chapter 1, we conducted experiments on four distinct tasks and examined the performance in terms of overall and temporal behavior. In this section, we will conclude our findings based on the results obtained and discuss the limitations of our findings. Additionally, we will propose potential future directions for researchers to explore further based on this work.

7-1 Conclusion

As stated in Chapter 1, we intend to address the current lack of consensus on the performance of the Kinetics EKF method facing the challenges of human motion analysis. In the experiments, we validated Kinetics EKF under different human motion tasks with the following challenges and conclusions:

The model has higher complexity in joint mechanisms. We use a kinetics model with ball and socket joints in the method Kinetics Extended Kalman Filter (EKF) and compare it to the benchmark Marker IK method, which provides reliable joint angle estimation. We find the RMSD between Kinetics EKF and Marker IK to be within 16° for joint angle estimation of all tasks, except for the Treadmill task. The joint angle estimation with the largest RMSD is for the distal joints. The RMSD for joint torque estimation is smaller than 3 Nm when Kinetics EKF is compared to Marker IK/ID for all tasks, except for the Treadmill task.

The joint load change on the human subject is more abrupt and frequent. During the MMH task, the external force input is generated by step signals produced while grabbing and placing the weight on the shelf. The Kinetics EKF rapidly reacts to changes in the external force, even capturing very slight motion detected by IMU, achieved by tuning the hyperparameters to adjust the joint torque estimation quickly. Notably, Marker

IK/ID could not capture that slight motion as it was filtered out during ID calculation. To enable simultaneous correction of joint velocity and joint torque predictions, the process noise covariance of joint velocity and joint torque need to be large. Additionally, we observed that IEKF can further improve the estimation accuracy, providing proper hyperparameter tuning and ensuring a fast and oscillation-free response in joint torque estimation.

The motion is highly dynamic and could face STA. The STA has no effects on the estimation results except for the Treadmill task, which is the most dynamic task we tested during the experiments. Through analysis, we conclude that during this task, the IMU measurements are highly susceptible to STA. The degradation in estimation accuracy in the Treadmill task was observed to occur after 60 seconds. The simulated IMU signal from Marker IK estimation revealed that the experimental IMU measurements have erroneous peaks in angular velocity measurements. Those peaks coincide with the instances when the joint velocity estimation is also erroneous. Therefore, we found that the Kinetics EKF is susceptible to STA.

Moreover, we have answered the following questions by comparing Kinetics EKF to Kinematics EKF and OpenSense:

Performance comparison between kinetics model and kinematics model In comparison to kinematics-based methods using the Dribbling task, Kinetics EKF is able to reduce the drifting and exhibits smaller RMSD for joint angle estimation with 11.33°, compared to Kinematics EKF with RMSD of 15.33°. The RMSD of joint angle estimation from OpenSense is smaller than Kinetics EKF with 1.23°. Notably, the absence of heading information in Kinetics EKF does not significantly impact estimation accuracy, setting it apart from OpenSense, which requires heading information. These findings highlight the promising potential of using the kinetics model for human motion estimation. Among these three methods, Kinetics EKF also yields the lowest RMSD in joint torque estimation of 2.31 Nm, whereas the RMSD for Kinematics EKF and OpenSense is 3.81 Nm and 2.65 Nm, respectively.

Differences between kinetics and kinematics model structure Kinetics EKF demonstrates inherent differences from Kinematics EKF, which solely relies on kinematics knowledge. By incorporating joint torque estimation and forward dynamics into the system model, the dynamics of the joint velocity become more meaningful. Additionally, the measurement model becomes denser compared to alternative methods. However, the inclusion of additional information also introduces more noise. We observe that the noisy input signal from the force sensor propagates into the joint torque estimation and impacts the prediction of IMU signals, possibly affecting estimation accuracy. This requires more careful consideration regarding the extra included information. This observation suggests changing the external force from being an input signal to being a part of the system measurements.

7-2   Limitations

Firstly, in this study, the noise covariance of the IMU measurements were calibrated based on the manufacturer's specifications without conducting dedicated experiments to assess realistic bias and noise covariance values. Additionally, the inclusion of bias as a part of the state for estimation was not implemented, despite the likelihood of bias changing over time during longer-duration trials. Therefore, in our experiments, we overestimated our trust in the measurements of IMU.

Secondly, the specific force measurements underwent casual low-pass filtering throughout the thesis. Towards the end of the research, it was discovered that certain frequency components related to contact on the rim might have been filtered out. However, this does not contradict our conclusion regarding the presence of STA during the Treadmill task or have a severe impact on our estimation accuracy.

7-3   Future Works

Model Parametrization The system model employed in this study adopts a structure with Euler angles as the state variables. However, our proposed framework has not yet been compared to methods that utilize a quaternion as the modeling parametrization. Considering the well-known limitations of gimbal locks associated with Euler angles, we recommend future researchers explore the possibility of utilizing quaternion or rotation matrix representations while also incorporating kinetics knowledge.

Filtering Technique In the context of estimation algorithms, for future work focusing on Euler angle-based parametrization, it is advisable to explore the application of the UKF for state estimation. The presence of nonlinearity in the current state estimation process suggests that the UKF could potentially offer improvements. Unlike other methods, the UKF does not necessitate the explicit computation of the Jacobian and Hessian matrices of the system. Instead, it leverages the unscented transform to address nonlinearity and enhance the estimation accuracy of highly nonlinear system models. For researchers utilizing quaternion and rotation matrix as parametrization methods as in the previous suggestion, MEKF are recommended.

Measurements/Input Model Based on our understanding of the system model's inherent bias, we propose that future studies explore the possibility of modifying the input external force signal within the measurement model. This modification would make the prediction step more impartial, enabling the correction step to comprehensively determine whether the external force should be counteracted through kinematics or kinetics in conjunction with the IMU measurements. In other words, if we understand this problem from the optimal control point of view, the joint torque will be the control signal and the external force works as an input disturbance to the system.

Propulsion Cycle Analysis In the case of the Treadmill task, a clear periodic pattern is evident. However, due to the specific focus of our testing on various tasks, we did not conduct an analysis specifically targeting the propulsion cycle of the Treadmill task. We recommend that future studies, particularly those in the field of biomechanics, analyze

the propulsion cycle for the Treadmill task using our proposed framework. It would also be beneficial to include data from multiple participants to assess the repeatability and consistency of our proposed framework.

Accessibility of the Framework In realistic scenarios, the reliance on external force measurements have reduced the applicability of our proposed method, as IMUs are unable to directly capture the influence of external forces. It would be intriguing to investigate the use of additional models or extra wearable sensors to estimate the external force, such as incorporating a contact model with contact-induced acceleration signals or electromyography measurements.

Validation Method It is well-known that marker IK/ID methods are susceptible to errors, including STA and alignment errors. For future investigations, it may be beneficial to address these types of errors by introducing variations in the virtual marker positions within a range of 1-2 cm. By using the results obtained within this range as a benchmark estimation, one can determine if the proposed method yields comparable estimations to marker IK/ID. This approach would provide valuable insights into the accuracy and reliability of the newly proposed method in relation to marker-based techniques.

Appendix A

Additional Results

A-1 Data Collection

To demonstrate the signal measured by Inertial Measurement Units (IMUs) on four different motions, Fig. A-1 provides the measurements of IMUs attached to the humerus. The first row represents specific force measurements, while the second row represents gyroscope measurements. We have zoomed into the specific time scale to demonstrate the level of the dynamic of the motion.

For Desk motion, the specific force and the angular velocity measurements are the highest during the "happy handshakes" motion. The Manual Material Handling (MMH) measurement exhibits peaks in Inertial Measurement Unit (IMU) measurements when the participant extends their arm to place and grab a weight from the highest shelves.

In comparison to Desk, Dribbling displays a higher dynamic range with the highest specific force and angular velocity measurements reaching $40m/s^2$ and $250°/s$, respectively. However, due to the motion constraints provided in Table 5-1, which limit the number of propulsion actions, no clear repetitive pattern is observed.

In contrast, during treadmill motion, participants can repeatedly engage in wheelchair propulsion, resulting in a discernible pattern of repetitive specific force and angular velocity measurements. The highest measurements reach approximately $50m/s^2$ and $400°/s$, respectively.

To further investigate the difference in pushing frequency, Fig. A-2 displays the time scales for Dribbling and Treadmill motion, both set to 35 seconds. It is concluded that the Treadmill results in a higher frequency of pushing and a steeper change in the force exerted on the rim. This combination of a higher rate of pushing and a relatively rapid change in the push force on the rim presents challenges in accurately estimating the motion during the Treadmill motion, as explained in detail in the subsequent sections.

During the MMH motion, the external force exerted on the hand is the previously measured gravity of a 2kg object. However, in our experiments, this external force has been artificially set to an abrupt step signal, rather than being directly measured.
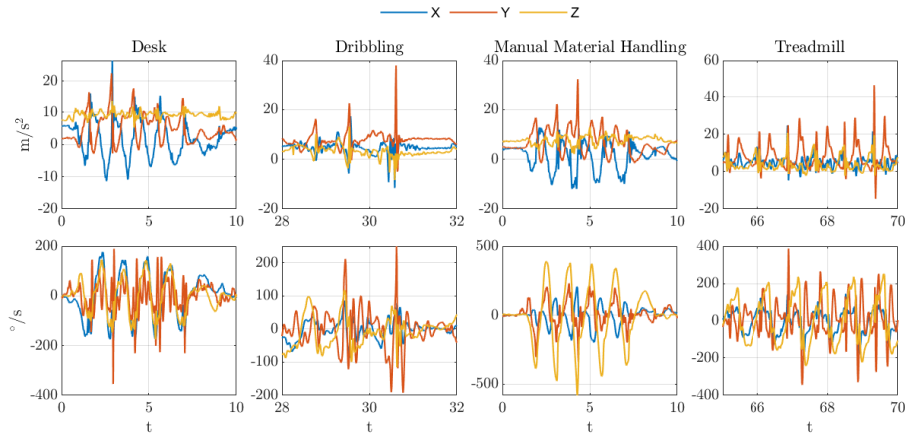
Figure A-1: The IMU measurements of four different motions. Specific force and angular velocity signals are represented in the first and second rows respectively.
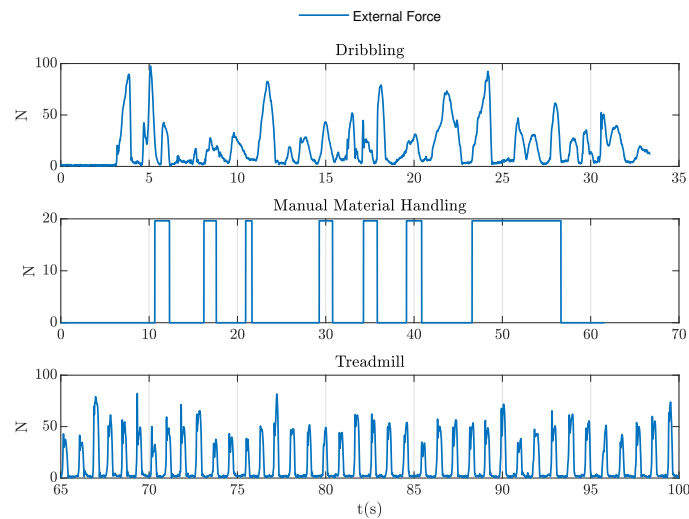

Figure A-2: Plot demonstrating the external force measurements used as input to the system. The external force for the task of Treadmill has been set to the time scale of 35 seconds.
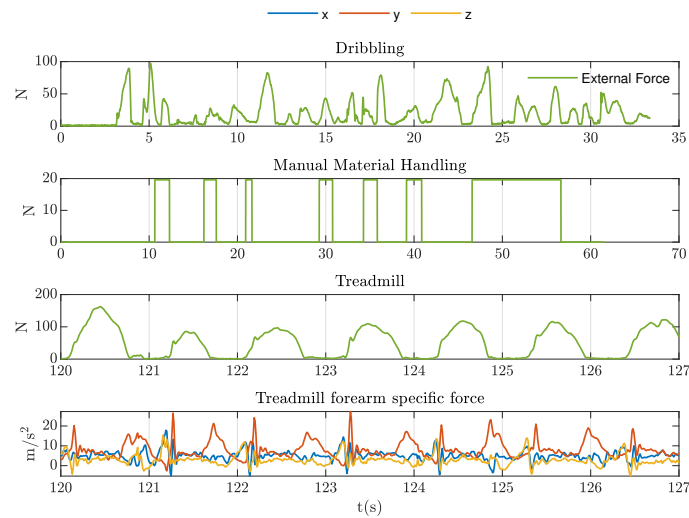
Figure A-3: External force measurement of three different motions on the time scale of 5 seconds.

A-2   Periodic Pattern of Treadmill Motion

The motions of MMH, Dribbling, and Treadmill all involve the application of external forces on the hand. Fig. A-3 provides a time plot showcasing the artificially set or measured external forces. Notably, the external force measurement for Treadmill motion is presented with a focused time scale of 5 seconds, with forearm-specific force measurements depicted in the last row. Upon comparing the wheelchair propulsion motions of the Dribbling and Treadmill, it is evident that the push forces exerted on the rim fall within a similar range. In the case of Treadmill motion, the periodic pattern is clearly exhibited by the specific force and external force measurements on the forearm and hand. The specific force exhibits peak values when the hand is in contact with the push rim and initiates force generation. While the force on the rim remains high, the specific force measurements primarily only capture the effect of gravity. As the hand disengages from the rim and no force is being exerted, the hand shifts towards the back of the body, leading to an increase in the specific force measurements.

A-3   Over all Root Mean Squared Difference (RMSD) for four tasks

To evaluate the performance of our proposed method in comparison to the baseline method, Marker Inverse Kinematics (IK), we summarize the resulting RMSD of the estimation for joint angle, joint velocity, and joint torque in Table A-1, A-2, and A-3, respectively. The iterative version of our method is represented in the Iterative Extended Kalman Filter (IEKF) column. Each cell in the tables corresponds to the RMSD of a specific joint throughout the entire motion trial. For visual clarity, we employ a color coding scheme where the interpolation of colors ranges from red (indicating the maximum RMSD in each table) to green (indicating the minimum RMSD). This color scheme enables effective comparison and assessment of RMSD differences among different joints, motions, and iteration times.

The results are based on the author's best hyperparameter tuning. The hyperparameters of the IEKF are set to be the same as the Extended Kalman Filter (EKF) for the each task.

Table A-1: The RMSD of angle estimation for all joints in four distinct motions.

Joint angle RMSD(°)	Desk		Dribbling		ManualMaterial		Treadmill
	EKF	IEKF	EKF	IEKF	EKF	IEKF	EKF
Thorax tilt	3.66	3.88	3.30	3.34	4.74	3.65	2.48
Thorax list	3.98	3.03	9.54	8.68	4.95	6.48	9.92
Thorax rotation	4.61	18.52	24.71	22.03	5.74	14.14	20.29
Shoulder flexion	20.06	11.76	10.02	8.81	12.35	17.81	29.16
Shoulder adduction	9.64	4.64	4.12	3.89	5.88	12.41	13.38
Shoulder rotation	4.14	8.89	6.94	5.97	22.23	12.28	34.77
Forearm flexion	23.03	23.14	14.44	14.78	19.79	20.69	37.58
Forearm rotation	41.94	42.18	28.17	29.16	26.35	26.23	18.79
Overall	15.13	14.50	12.65	12.08	12.75	14.21	20.79

Table A-2: The RMSD of velocity estimation for all joints in four distinct motions.

Joint velocity RMSD(°/s)	Desk		Dribbling		ManualMaterial		Treadmill
	EKF	IEKF	EKF	IEKF	EKF	IEKF	EKF
Thorax tilt	3.25	3.40	7.45	7.30	7.91	7.72	10.34
Thorax list	4.86	4.82	8.37	8.05	7.48	7.93	11.65
Thorax rotation	5.72	5.72	6.84	6.79	10.73	11.02	9.25
Shoulder flexion	63.74	56.46	17.96	17.53	75.27	60.40	76.12
Shoulder adduction	20.31	18.55	15.27	14.22	20.89	23.52	55.69
Shoulder rotation	73.66	73.47	29.01	28.71	89.67	64.73	98.83
Forearm flexion	27.08	27.10	16.73	16.67	27.64	27.45	46.29
Forearm rotation	53.12	53.16	41.76	41.90	69.90	69.54	113.30
Overall	31.47	30.33	17.92	17.65	38.69	34.03	52.68

Table A-3: The RMSD of torque estimation for all joints in four distinct motions.

Joint torque RMSD(Nm)	Desk		Dribbling		ManualMaterial		Treadmill
	EKF	IEKF	EKF	IEKF	EKF	IEKF	EKF
Thorax tilt	4.11	6.45	6.94	6.49	5.22	6.41	7.86
Thorax list	3.37	3.55	6.27	5.76	5.72	6.41	7.46
Thorax rotation	1.89	1.99	2.30	2.14	3.33	3.34	7.63
Shoulder flexion	1.10	0.89	2.02	1.96	2.18	2.37	7.28
Shoulder adduction	2.37	1.29	2.11	2.01	1.71	2.32	7.64
Shoulder rotation	0.44	0.45	0.88	0.81	1.81	1.81	2.33
Forearm flexion	0.39	0.40	1.38	1.28	1.39	1.41	3.42
Forearm rotation	0.06	0.06	0.07	0.06	0.32	0.32	0.23
Overall	1.72	1.89	2.75	2.56	2.71	3.05	5.48

Based on the analysis presented in Table A-1, it is apparent that the distal joint demonstrates a higher RMSD for joint angle estimation compared to the proximal joint. However, in Table A-3, this trend is reversed, indicating a different behavior. This observation can be attributed to the inherent modeling strategy employed in OpenSim, which follows a chain model structure. Consequently, the proximal joints have an influence on the IMU measurements of the distal segments. In the subsequent section, we will delve into the temporal characteristics of these four distinct motions.

A-4   Assessing the Time-Dependent Mean Absolute Difference (MD) of Joint Angle Estimation

By examining the time-dependent pattern we aim to identify the influence of integration drift exists in our method. We observed higher RMSD values specifically in thorax rotation, shoulder flexion, shoulder rotation, and forearm rotation, as indicated in Table A-1. The MD of the proposed method compared to Marker IK is illustrated in Fig. A-4 for the aforementioned joints. The MD was computed every 5 seconds for each motion and is represented by the blue dots. The red line corresponds to a linear fit of the computed MD data to indicate the increasing/decreasing trends, with the slope denoted as m. It should be noted that when evaluating the MD between our method and Marker IK, the slope of the error can indicate a non-constant difference between the two methods, regardless of whether it is positive or negative. This slope serves as an indication of the presence of drift in our method.

Firstly, it is evident that during the Desk motion, the joint angle estimation for forearm rotation exhibits clear drifting over time, particularly noticeable in the upper right corner of the plot. Similarly, the drifting behavior in thorax rotation is quite pronounced during the initial thirty seconds. Even the forearm flexion joint, which is typically considered less affected by the loss of heading information, shows a drift of 15° within 40 seconds. Drifting tendencies can also be observed for the forearm flexion joints during the MMH motion, with a noticeable approximate 15° change over time. However, it is possible that this performance could be further improved by tuning the hyperparameter.
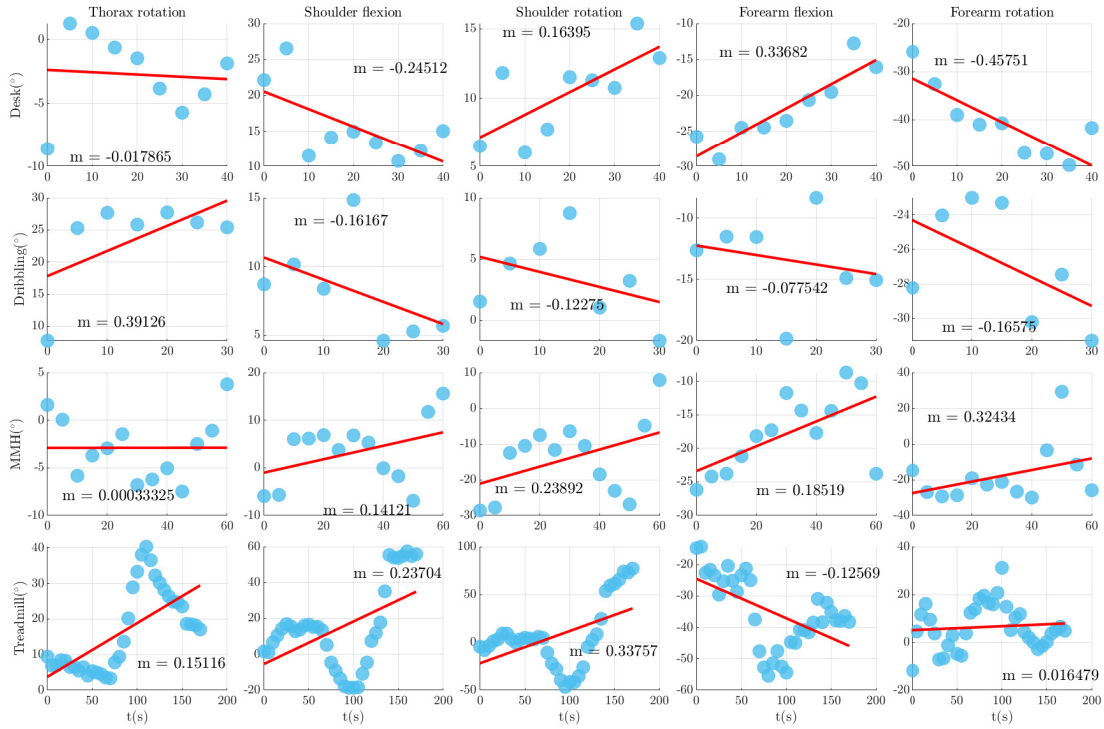
Figure A-4: Temporal variation of MD over time for five selected joints and four motions. The blue dots represent the MD of five-second durations consecutively.

Secondly, the impact of integration drift is less apparent during the Dribbling motion, where the MD appear more constant compared to the other three motions. In the joint of thorax rotation, the MD exhibits an almost constant value starting from 5 seconds.

Thirdly, the plot depicting the MD as a function of time provides a clear visualization of the vulnerability of the Treadmill motion to drift over time, particularly in the thorax rotation and shoulder rotation joints. However, it is worth noting that the changing trends of the MD exhibit fluctuations and become more pronounced only after 60 seconds and 100 seconds, suggesting the existence of additional error sources that influence the accuracy of estimation. A more detailed investigation of this behavior will be carried out in the forthcoming sections.

A-5   Additional Results for Experimental Validation on Highly Dynamic Motion

In the case of Treadmill motion, despite the absence of artificially set step signals in the input signal, the rate of change in the external force signal remains steep. Upon contact with the rim, the hand instantaneously generates a significant force, surpassing the force induced by the dumbbell in MMH motion. This observation is clearly depicted in Fig. A-3, where the initial spike reaches a magnitude of 160N within a half-second interval. In order to mitigate the tendency to artificially increase the joint velocity to compensate for the input external force, appropriate measures have been taken. The specific tuning configuration is detailed in Table A-4, where the parameter Q_f is set larger compared to previous motions. Additionally,

to ensure system stability, Q_τ is set smaller than in Desk and Dribbling motion but larger than in MMH motion. It is worth noting that setting both Q_f and Q_τ excessively large would transform the system into a nonlinear least square problem, rendering it susceptible to instability.

Table A-4: Table of hyperparameter setting for the Treadmill motion.

Method	Measurement Noise						Process Noise		
	R_{s,a_1}	R_{s,ω_1}	R_{s,a_2}	R_{s,ω_2}	R_{s,a_3}	R_{s,ω_3}	Q_q	Q_f	Q_τ
EKF	2.59×10^1	4.04×10^{-3}	2.59×10^1	4.04×10^{-1}	2.59×10^1	4.04×10^{-1}	1×10^{-6}	1×10^5	1×10^5

This particular tuning configuration yields the lowest RMSD for joint angle and joint torque estimation among the investigated hyperparameters in this study. However, despite the reduced occurrence of drifting behavior compared to other settings, the estimation still falls short of being satisfactory. As depicted in Fig. A-4, the MD fluctuates by up to 100° over a 170-second duration, highlighting the challenges associated with Treadmill motion. To investigate the reason of low estimation accuracy, three additional tuning scenarios, denoted as s1, s2, s3, and s4, are introduced with consistent settings for the measurement noise covariance. These scenarios, along with their respective tuning configurations, are presented as $\begin{bmatrix} Q_f \\ Q_\tau \end{bmatrix} = \begin{bmatrix} 1 \times 10^5 \\ 1 \times 10^5 \end{bmatrix}$, $\begin{bmatrix} Q_f \\ Q_\tau \end{bmatrix} = \begin{bmatrix} 1 \times 10^4 \\ 1 \times 10^8 \end{bmatrix}$, $\begin{bmatrix} Q_f \\ Q_\tau \end{bmatrix} = \begin{bmatrix} 1 \times 10^2 \\ 1 \times 10^8 \end{bmatrix}$, and $\begin{bmatrix} Q_f \\ Q_\tau \end{bmatrix} = \begin{bmatrix} 1 \times 10^{-6} \\ 1 \times 10^8 \end{bmatrix}$, respectively.

By progressively increasing the value of Q_f from s4 to s1, we aim to amplify the mistrust in joint velocity prediction. Conversely, in s1, we decreased Q_τ compared to the other scenarios to dampen the responsiveness of joint torque estimation. The evaluation of these four scenarios is summarized in Table A-5, which clearly demonstrates that s1 achieved the lowest RMSD values for joint angle and joint torque estimation, but exhibited the largest RMSD in IMU signal prediction.

Table A-5: The RMSD for 4 different hyperparameter tunning scenarios.

Scenarios	Joint Angle RMSD(°)	Joint Velocity RMSD(°/s)	Joint Torque RMSD(Nm)	Specific Force RMSD(m/s²)	Angular Velocity RMSD(°/s)
s1	20.79	52.64	5.48	6.80	33.34
s2	27.46	65.62	7.38	2.93	19.65
s3	37.74	63.79	6.36	1.36	15.42
s4	45.29	65.65	5.59	1.32	15.70

To further analyze the behavior of the system, Fig. A-5 presents the MD of the four settings, focusing on thorax rotation, shoulder flexion, and shoulder rotation joints, which exhibited noticeable drifting. Notably, the drifting behavior in s1 and s3 began around 60 seconds, with another turning point occurring around 100 seconds, coinciding with increases in treadmill speed and inclination. Among the drifting joints, shoulder rotation showed the most severe drift.

To investigate the joint velocity estimation, Fig. A-6 provides a zoomed-in time interval of around 60 seconds, particularly in relation to shoulder rotation. The rows display joint
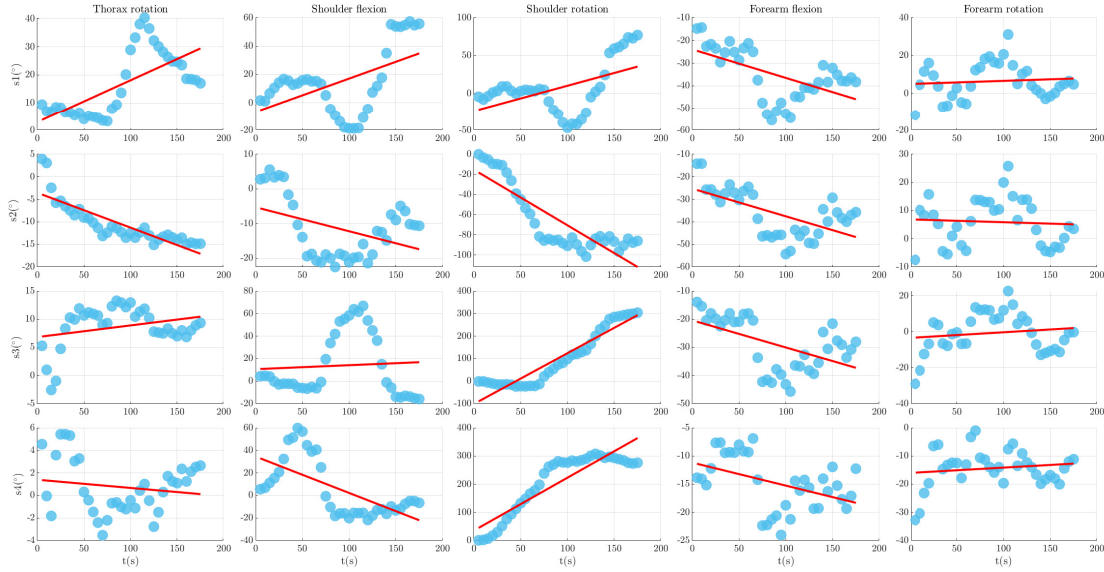
Figure A-5: MD of the Treadmill motion for 4 different setting scenarios on 5 joints.

velocity, joint angle, joint torque, and external force signal, respectively. It is evident that the joint velocity estimation does not align well with the results obtained from Marker IK, exhibiting intermittent mysterious peaks. While the reliability of differentiating Marker IK for joint velocity estimation remains debatable, the more frequent peaks in Kinetics EKF estimation compared to the non-drifting Marker IK estimation contribute to the drifting observed in joint angle estimation. The gray vertical lines in the figure highlight the occurrence of these mysterious peaks at specific time instances (t = 67.39, 68.19, 68.97, 69.81, and 70.65 seconds).

Regarding joint torque estimation, we found that s2, s3, and s4 exhibited greater responsiveness compared to s1 due to the higher value of Q_τ. In contrast, the joint torque estimation from s1 consistently displayed a noticeable delay.

A-5-1   Simulated IMU Signal for Treadmill Motion

Figure A-7 visually depicts the RMSD between the measured IMU signal vector and the predicted IMU signal vector. Each circle on the plot represents the RMSD within each 5-second interval represented by the blue circle through the trial. It is notable that the RMSD shows an increase at 60 and 100 seconds, corresponding to the onset of drifting. Surprisingly, scenario s2 and s1, which features the higher process covariance Q_f, exhibits higher RMSD values compared to s3 and s4, particularly in the forearm IMU signal. In contrast, Table A-5 reveals a smaller the RMSD for joint angle estimation of s1 and s2. This observation suggests that certain components of the IMU measurements are not highly reliable.

A-5-2   Condition of EKF Algorithm during Treadmill Motion

According to the study by McGrath et al. [36], the absence of heading information in human motion estimation can introduce non-identifiable variables in the system when the measured
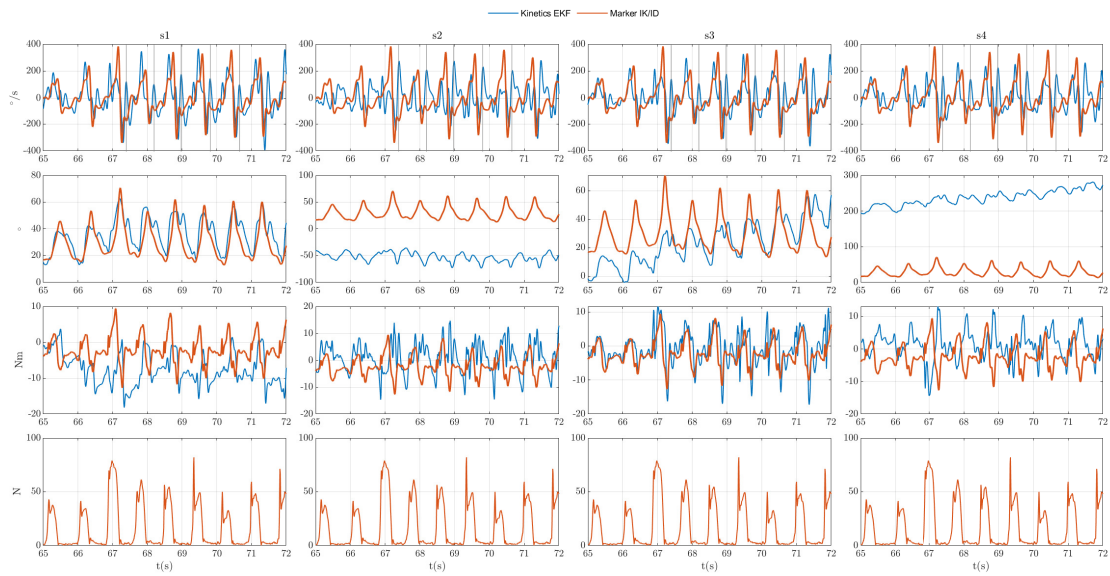
Figure A-6: Fine-scaled Treadmill motion estimation of 4 different setting for joint velocity, angle, and torque.
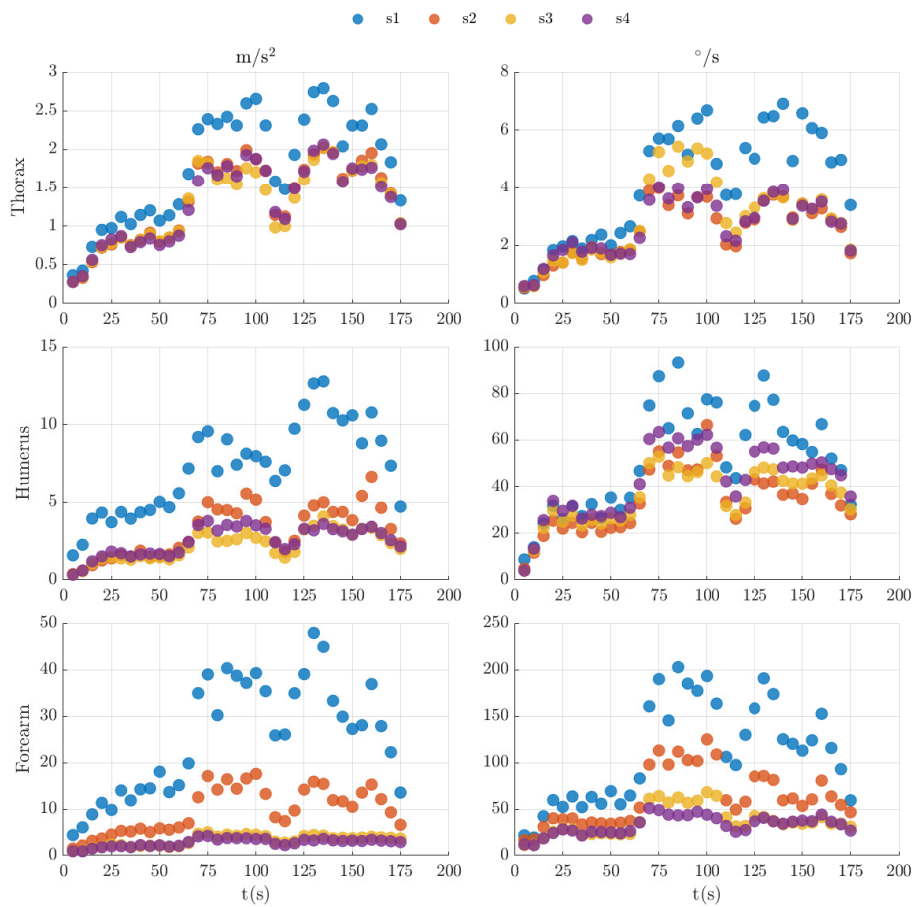

Figure A-7: The plot of averaged IMUs signal composed from three axis of every 5 second with the averaged reprojection error also composed from three axis.

signal lacks sufficient excitation. They observed that when the static vectors connecting the IMU to adjacent joint centers are predominantly vertical, perpendicular to the heading plane, the orientation trajectory of the IMU becomes underconstrained. Consequently, multiple solutions with constant offsets in heading become possible. This situation can arise during activities such as upright walking with short step lengths. Considering that our measurements also lack heading information and the behavior of the shoulder joint exhibits a similar pattern of the hip joint as described in their study, our objective is to utilize the Hessian matrix and its corresponding condition number to investigate the presence of non-identifiable parameters.
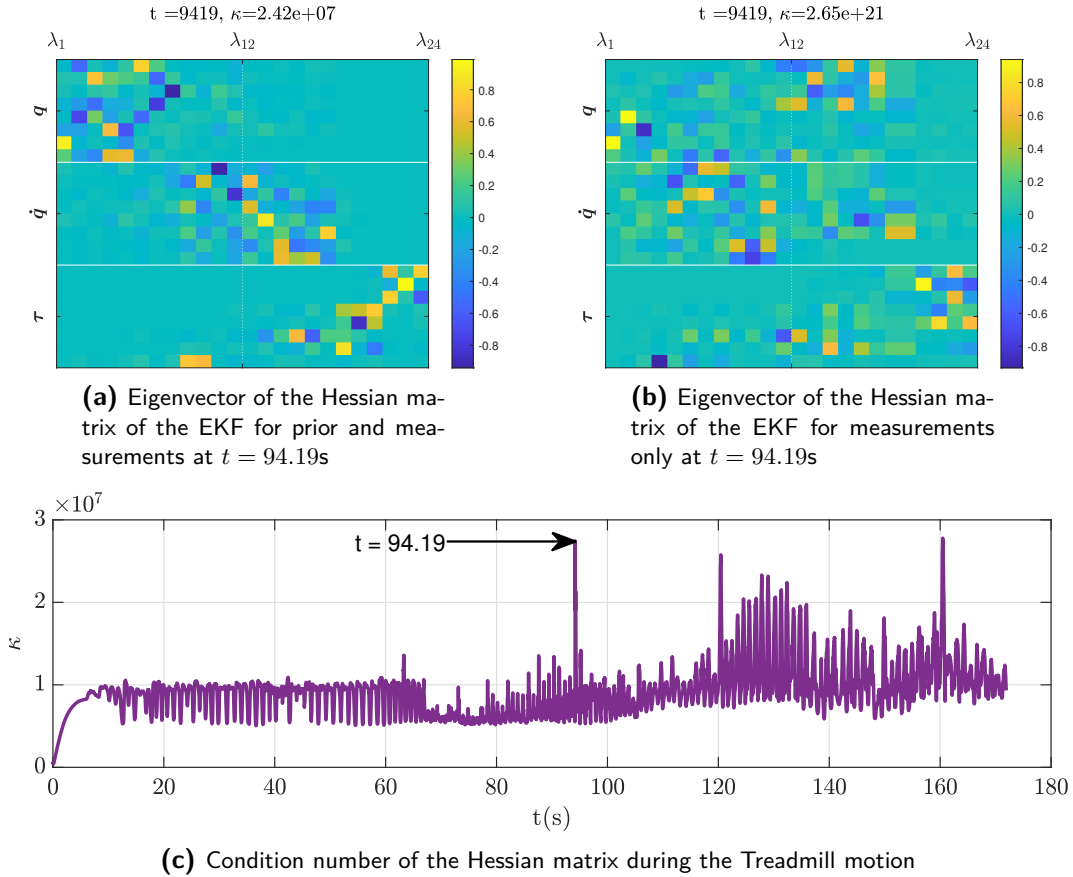

(a) Eigenvector of the Hessian matrix of the EKF for prior and measurements at $t = 94.19$s

(b) Eigenvector of the Hessian matrix of the EKF for measurements only at $t = 94.19$s

(c) Condition number of the Hessian matrix during the Treadmill motion

Figure A-8: Hessian matrix analysis for EKF during Treadmill motion.

In Fig. A-8, the parameter κ represents the condition number of the Hessian matrix. A high condition number indicates that our filter estimation is ill-conditioned, suggesting the possibility of non-identifiable variables in the system. Throughout the trial, the condition number demonstrates a pulsatile behavior with a frequency corresponding to the propulsion cycle. This indicates that the excitation signal from the measurements and input influences the behavior of the estimation algorithm. However, even with the highest condition number observed in the trial, we have concluded that the variables in our system remain identifiable based on analyzing the Hessian matrix. The magnitude of 10^7 for the condition number falls within a reasonable range based on our predetermined settings for the hyper-parameters of process and measurement noise covariance in Table A-4.

We further examined the time when the peak value of the condition number was observed

during the experiment. In Fig. A-8a, we present a heat map of the eigenvectors of the Hessian matrix of the EKF at t= 94.19 s. Each column in the heatmap represents an eigenvector, ordered from the largest eigenvalue λ_1 to the smallest eigenvalue λ_{24}. Similarly, Fig. A-8b displays the same content but with only the measurements included in the optimization cost function.

It is noteworthy that when only the measurement is used, the condition number significantly increases and exceeds the reasonable range for ensuring the identifiability of all variables. This demonstrates that without a reliable prior prediction, we are not able to estimate the states of the system. Additionally, the directions corresponding to the eigenvalues appear chaotic and point in arbitrary directions. However, upon incorporating the prior knowledge, we observe that the directions with large curvature, characterized by large eigenvalue or smaller covariance values, align with the joint angle and angular velocity. In contrast, the smallest eigenvalue is pointing in the direction of joint torque, which means its estimation appears flatter and exhibits larger covariance values. This corresponds to our choice of using a larger covariance value for the process noise of joint torque to allow for flexible adjustments and tracking of the measurement signal.

With the inclusion of prior knowledge, the condition number of the Hessian matrix considerably decreases, indicating that the system is not considered non-identifiable. Instead, the presence of unreliable estimation from the prediction step is hindering the estimation from converging to the global optimum.

Bibliography

[1] S. A. Rawashdeh, D. A. Rafeldt, and T. L. Uhl, "Wearable imu for shoulder injury prevention in overhead sports," *Sensors*, vol. 16, no. 11, p. 1847, 2016.

[2] A. Kondo, H. Doki, and K. Hirose, "An attempt of a new motion measurement method for alpine ski turns using inertial sensors," *Procedia Engineering*, vol. 34, pp. 421–426, 2012.

[3] D. B. Chaffin, "On simulating human reach motions for ergonomics analyses," *Human Factors and Ergonomics in Manufacturing & Service Industries*, vol. 12, no. 3, pp. 235–247, 2002.

[4] F. Caputo, A. Greco, E. D 'Amato, I. Notaro, and S. Spada, "Imu-based motion capture wearable system for ergonomic assessment in industrial environment," in *Advances in Human Factors in Wearable Technologies and Game Design: Proceedings of the AHFE 2018 International Conferences on Human Factors and Wearable Technologies, and Human Factors in Game Design and Virtual Environments, Held on July 21–25, 2018, in Loews Sapphire Falls Resort at Universal Studios, Orlando, Florida, USA 9*, pp. 215–225, Springer, 2019.

[5] E. Digo, L. Gastaldi, M. Antonelli, S. Pastorelli, A. Cereatti, and M. Caruso, "Real-time estimation of upper limbs kinematics with imus during typical industrial gestures," *Procedia Computer Science*, vol. 200, pp. 1041–1047, 2022.

[6] D. A. Winter, *Biomechanics and motor control of human movement.* John wiley & sons, 2009.

[7] A. Cappozzo, U. Della Croce, A. Leardini, and L. Chiari, "Human movement analysis using stereophotogrammetry: Part 1: theoretical background," *Gait & posture*, vol. 21, no. 2, pp. 186–196, 2005.

[8] M. Kok, J. D. Hol, and T. B. Schön, "Using inertial sensors for position and orientation estimation," *Foundations and Trends in Signal Processing*, vol. 11, no. 1-2, pp. 1–153, 2017.

[9] T. Piazza, J. Lundström, A. Kunz, and M. Fjeld, "Predicting missing markers in real-time optical motion capture," in *Modelling the Physiological Human: 3D Physiological Human Workshop, 3DPH 2009, Zermatt, Switzerland, November 29–December 2, 2009. Proceedings*, pp. 125–136, Springer, 2009.

[10] F. C. Van der Helm, "A finite element musculoskeletal model of the shoulder mechanism," *Journal of biomechanics*, vol. 27, no. 5, pp. 551–569, 1994.

[11] M. El-Gohary and J. McNames, "Human joint angle estimation with inertial sensors and validation with a robot arm," *IEEE Transactions on Biomedical Engineering*, vol. 62, no. 7, pp. 1759–1767, 2015.

[12] M. Miezal, B. Taetz, and G. Bleser, "On inertial body tracking in the presence of model calibration errors," *Sensors*, vol. 16, no. 7, p. 1132, 2016.

[13] V. Joukov, J. Ćesić, K. Westermann, I. Marković, D. Kulić, and I. Petrović, "Human motion estimation on lie groups using imu measurements," in *2017 IEEE/RSJ International Conference on Intelligent Robots and Systems (IROS)*, pp. 1965–1972, IEEE, 2017.

[14] I. Weygers, M. Kok, H. De Vroey, T. Verbeerst, M. Versteyhe, H. Hallez, and K. Claeys, "Drift-free inertial sensor-based joint kinematics for long-term arbitrary movements," *IEEE Sensors Journal*, vol. 20, no. 14, pp. 7969–7979, 2020.

[15] M. Kok, J. D. Hol, and T. B. Schön, "An optimization-based approach to human body motion capture using inertial sensors," *IFAC Proceedings Volumes*, vol. 47, no. 3, pp. 79–85, 2014.

[16] T. McGrath and L. Stirling, "Body-worn imu-based human hip and knee kinematics estimation during treadmill walking," *Sensors*, vol. 22, no. 7, p. 2544, 2022.

[17] M. Kok, K. Eckhoff, I. Weygers, and T. Seel, "Observability of the relative motion from inertial data in kinematic chains," *Control Engineering Practice*, vol. 125, p. 105206, 2022.

[18] E. Dorschky, M. Nitschke, A.-K. Seifer, A. J. van den Bogert, and B. M. Eskofier, "Estimation of gait kinematics and kinetics from inertial sensor data using optimal control of musculoskeletal models," *Journal of biomechanics*, vol. 95, p. 109278, 2019.

[19] D. de Kanter, "An imu tracking algorithm for 3d motion reconstruction using opensim dynamical models: Implementation on a robot manipulator," 2021.

[20] M. A. Skoglund, Z. Sjanic, and M. Kok, "On orientation estimation using iterative methods in euclidean space," in *2017 20th International Conference on Information Fusion (Fusion)*, pp. 1–8, IEEE, 2017.

[21] T. Drummond, "Lie groups, lie algebras, projective geometry and optimization for 3d geometry, engineering and computer vision," 2014.

[22] G. Bourmaud, R. Mégret, M. Arnaudon, and A. Giremus, "Continuous-discrete extended kalman filter on matrix lie groups using concentrated gaussian distributions," *Journal of Mathematical Imaging and Vision*, vol. 51, pp. 209–228, 2015.

[23] S. O. Madgwick, A. J. Harrison, and R. Vaidyanathan, "Estimation of imu and marg orientation using a gradient descent algorithm," in *2011 IEEE international conference on rehabilitation robotics*, pp. 1–7, IEEE, 2011.

[24] R. Mahony, T. Hamel, and J.-M. Pflimlin, "Nonlinear complementary filters on the special orthogonal group," *IEEE Transactions on automatic control*, vol. 53, no. 5, pp. 1203–1218, 2008.

[25] L. Tagliapietra, L. Modenese, E. Ceseracciu, C. Mazzà, and M. Reggiani, "Validation of a model-based inverse kinematics approach based on wearable inertial sensors," *Computer Methods in Biomechanics and Biomedical Engineering*, vol. 21, no. 16, pp. 834–844, 2018.

[26] M. Al Borno, J. O'Day, V. Ibarra, J. Dunne, A. Seth, A. Habib, C. Ong, J. Hicks, S. Uhlrich, and S. Delp, "Opensense: An open-source toolbox for inertial-measurement-unit-based measurement of lower extremity kinematics over long durations," *Journal of neuroengineering and rehabilitation*, vol. 19, no. 1, pp. 1–11, 2022.

[27] A. Karatsidis, M. Jung, H. M. Schepers, G. Bellusci, M. de Zee, P. H. Veltink, and M. S. Andersen, "Musculoskeletal model-based inverse dynamic analysis under ambulatory conditions using inertial motion capture," *Medical engineering & physics*, vol. 65, pp. 68–77, 2019.

[28] J. R. Cardoso, L. M. Pereira, M. D. Iversen, and A. L. Ramos, "What is gold standard and what is ground truth?," *Dental press journal of orthodontics*, vol. 19, pp. 27–30, 2014.

[29] T. K. Uchida and A. Seth, "Conclusion or illusion: Quantifying uncertainty in inverse analyses from marker-based motion capture due to errors in marker registration and model scaling," *Frontiers in Bioengineering and Biotechnology*, vol. 10, p. 874725, 2022.

[30] N. M. Fiorentino, P. R. Atkins, M. J. Kutschke, J. M. Goebel, K. B. Foreman, and A. E. Anderson, "Soft tissue artifact causes significant errors in the calculation of joint angles and range of motion at the hip," *Gait & posture*, vol. 55, pp. 184–190, 2017.

[31] J. Boelens, "Sensor fusion for estimating joint kinematics and kinetics of biomechanical systems: Validation using a robotic manipulator," 2022.

[32] V. Zatsiorsky, "Methods of determing mass-inertial characteristics of human body segments," *Contemporasy Problems of Biomechnics*, 1990.

[33] S. L. Delp, F. C. Anderson, A. S. Arnold, P. Loan, A. Habib, C. T. John, E. Guendelman, and D. G. Thelen, "Opensim: open-source software to create and analyze dynamic simulations of movement," *IEEE transactions on biomedical engineering*, vol. 54, no. 11, pp. 1940–1950, 2007.

[34] J. Sola, J. Deray, and D. Atchuthan, "A micro lie theory for state estimation in robotics," *arXiv preprint arXiv:1812.01537*, 2018.

[35] D. Roetenberg, H. Luinge, and P. Slycke, "Xsens mvn: Full 6dof human motion tracking using miniature inertial sensors," *Xsens Motion Technologies BV, Tech. Rep*, vol. 1, pp. 1–7, 2009.

[36] T. McGrath and L. Stirling, "Body-worn imu human skeletal pose estimation using a factor graph-based optimization framework," *Sensors*, vol. 20, no. 23, p. 6887, 2020.

[37] F. R. Kschischang, B. J. Frey, and H.-A. Loeliger, "Factor graphs and the sum-product algorithm," *IEEE Transactions on information theory*, vol. 47, no. 2, pp. 498–519, 2001.

[38] G. Wu, F. C. Van der Helm, H. D. Veeger, M. Makhsous, P. Van Roy, C. Anglin, J. Nagels, A. R. Karduna, K. McQuade, X. Wang, *et al.*, "Isb recommendation on definitions of joint coordinate systems of various joints for the reporting of human joint motion—part ii: shoulder, elbow, wrist and hand," *Journal of biomechanics*, vol. 38, no. 5, pp. 981–992, 2005.

[39] A. Rajagopal, C. L. Dembia, M. S. DeMers, D. D. Delp, J. L. Hicks, and S. L. Delp, "Full-body musculoskeletal model for muscle-driven simulation of human gait," *IEEE transactions on biomedical engineering*, vol. 63, no. 10, pp. 2068–2079, 2016.

[40] M. Miezal, G. Bleser, N. Schmitz, and D. Stricker, "A generic approach to inertial tracking of arbitrary kinematic chains," in *Proceedings of the 8th international conference on body area networks*, pp. 189–192, 2013.

[41] M. El-Gohary and J. McNames, "Shoulder and elbow joint angle tracking with inertial sensors," *IEEE Transactions on Biomedical Engineering*, vol. 59, no. 9, pp. 2635–2641, 2012.

[42] R. P. Matthew, S. Seko, and R. Bajcsy, "Fusing motion-capture and inertial measurements for improved joint state recovery: An application for sit-to-stand actions," in *2017 39th Annual International Conference of the IEEE Engineering in Medicine and Biology Society (EMBC)*, pp. 1893–1896, IEEE, 2017.

[43] M. Damsgaard, J. Rasmussen, S. T. Christensen, E. Surma, and M. De Zee, "Analysis of musculoskeletal systems in the anybody modeling system," *Simulation Modelling Practice and Theory*, vol. 14, no. 8, pp. 1100–1111, 2006.

[44] P. Slade, A. Habib, J. L. Hicks, and S. L. Delp, "An open-source and wearable system for measuring 3d human motion in real-time," *IEEE Transactions on Biomedical Engineering*, vol. 69, no. 2, pp. 678–688, 2021.

[45] G. Besançon, "A link between output time derivatives and persistent excitation for nonlinear observers," *IFAC-PapersOnLine*, vol. 49, no. 18, pp. 493–498, 2016.

[46] G. Wahba, "A least squares estimate of satellite attitude," *SIAM review*, vol. 7, no. 3, pp. 409–409, 1965.

[47] A. Seth, J. L. Hicks, T. K. Uchida, A. Habib, C. L. Dembia, J. J. Dunne, C. F. Ong, M. S. DeMers, A. Rajagopal, M. Millard, *et al.*, "Opensim: Simulating musculoskeletal dynamics and neuromuscular control to study human and animal movement," *PLoS computational biology*, vol. 14, no. 7, p. e1006223, 2018.

[48] W. Wu, P. V. Lee, A. L. Bryant, M. Galea, and D. C. Ackland, "Subject-specific musculoskeletal modeling in the evaluation of shoulder muscle and joint function," *Journal of biomechanics*, vol. 49, no. 15, pp. 3626–3634, 2016.

[49] "How forward dynamics works - opensim documentation." `https://simtk-confluence.stanford.edu:8443/display/OpenSim/How+Forward+Dynamics+Works`, Jul 2022.

[50] C. K. Liu and S. Jain, "A quick tutorial on multibody dynamics," *Online tutorial, June*, p. 7, 2012.

[51] B. M. Bell and F. W. Cathey, "The iterated kalman filter update as a gauss-newton method," *IEEE Transactions on Automatic Control*, vol. 38, no. 2, pp. 294–297, 1993.

[52] C.-T. Chen, *Linear system theory and design.* Saunders college publishing, 1984.

[53] Y. Mo, "Lecture 2: State estimation and kalman filter." `https://yilinmo.github.io/public/cds270/lecture02.pdf`, 2015.

[54] M. Schmidt, "Deriving the gradient and hessian of linear and quadratic functions in matrix notation." Department of Computer Science,University of British Columbia, February 6 2019.

[55] Shimmer 2016 Realtime Technologies Ltd, *IMU User Guide Revision 1.4*, 2016.

[56] W. H. de Vries, S. Amrein, U. Arnet, L. Mayrhuber, C. Ehrmann, and H. Veeger, "Classification of wheelchair related shoulder loading activities from wearable sensor data: A machine learning approach," *Sensors*, vol. 22, no. 19, p. 7404, 2022.